Novel Method for Monitoring the Electrochemical Capacitance by In Situ Impedance Spectroscopy as Indicator for Particle Cracking of Nickel-Rich NCMs: Part I. Theory and Validation

Journal of The Electrochemical Society, 2020 **167** 100511

Novel Method for Monitoring the Electrochemical Capacitance by In Situ Impedance Spectroscopy as Indicator for Particle Cracking of Nickel-Rich NCMs: Part I. Theory and Validation

Stefan Oswald,[*,z] Daniel Pritzl, Morten Wetjen, and Hubert A. Gasteiger[**]

Chair of Technical Electrochemistry, Department of Chemistry and Catalysis Research Center, Technical University of Munich, D-85748 Garching, Germany

Nickel-rich NCM ($LiMO_2$, with M = Ni, Co, and Mn) cathode active materials for lithium-ion batteries are being increasingly commercialized due to their high specific capacity. However, their capacity retention upon cycling is impaired by crack formation of NCM secondary agglomerates induced by the volume change upon repeated (de)lithiation that depends on the nickel content and the cutoff potential. Particle cracking leads to loss of electrical contact and enhanced side reactions caused by an increased surface area. Here, we introduce a novel method based on electrochemical impedance spectroscopy (EIS) in blocking conditions to quantify the increase in the active material's surface area upon cycling, utilizing the correlation between the surface area of the electrode and the electrochemical double-layer capacitance that is validated experimentally by comparing the capacitance and BET surface area increase of NCM electrodes upon mechanical compression. To quantify the cracking of the particles upon 200 charge/discharge cycles, we perform in situ EIS measurements utilizing a micro-reference electrode and monitor the cathode's impedance response. In addition, the crack formation of cycled NCM particles is validated visually by post mortem FIB-SEM. The effect of volume change on cracking is illuminated through the analysis of LFP and LTO as model materials.

 [DOI: 10.1149/1945-7111/ab9187]

Manuscript submitted April 2, 2020; revised manuscript received May 4, 2020. Published June 3, 2020.

Supplementary material for this article is available online

Layered lithium nickel cobalt manganese oxide based materials (NCMs, $Li_{1+\delta}Ni_xCo_yMn_zO_2$, $x+y+z+\delta = 1$) are commercially used cathode active materials (CAMs) in current lithium-ion batteries for electric vehicle applications,[1–3] owing to their technological maturity as well as their relatively high discharge capacity and discharge potential, resulting in superior energy and power density. To push the delivered specific capacity at the same upper cutoff potential closer to the theoretical limit of ~275 mAh/g_{NCM}, the nickel content of these materials is increased to values of $x > 0.8$. The increased nickel content, however, implies a lower thermal stability, compromised safety, a lower onset potential for oxygen release, and a shorter cycle life.[3–5]

One proposed failure mechanism of nickel-rich NCMs is the structural degradation of the NCM particles and the electrode due to volumetric changes of the rhombohedral unit cell upon repeated (de)lithiation of the NCM crystallites.[6] De Biasi et al. showed by in situ X-ray diffraction that the volume change of the NCM unit cell increases with the nickel content.[7] In addition, the unit cell volume changes anisotropically due to the unequal variation of the *a*- and the *c*-axis lattice parameter, leading to changes in the *c*/*a* ratio upon (de)lithiation that are accompanied by severe stress and strain in the particle, and, therefore, to an even stronger evolution of cracks in the secondary agglomerates.[6–8] Many studies have visually shown the formation of cracks upon extended charge/discharge cycling in nickel-rich NCMs[6,9–13] and NCAs,[9,14–17] accompanied by an increase in specific surface area (i.e. in BET surface area) and by the penetration of electrolyte into the secondary particle, exposing the primary NCM particles to the electrolyte.[14] It is expected that the formation of cracks in the polycrystalline material enhances the degradation of NCM cycle life by various mechanisms: (i) the release of lattice oxygen at the freshly exposed electrode/electrolyte interface can result in the formation of a rock-salt layer that hinders lithium diffusion,[8,9,14,18,19] (ii) the reaction of the simultaneously released singlet oxygen with the electrolyte constituents produces HF[20,21] that enhances active material loss due to transition metal dissolution,[22–24] and (iii) the eventual separation of fragments from the initial secondary NCM agglomerate, promoting loss of electrical contact of the active material.[6,16,25–27] Either one or a combination of these mechanisms will ultimately lead to increasing overpotentials and/or a loss of available capacity, limiting the discharge capacity of the cells.

Crack formation, either due to volume change upon electrochemical (de)lithiation[6,7] or due to mechanical compression upon calendering,[28,29] may have serious consequences with regard to cycle life—in particular, for CAMs having tailored surfaces to protect the sensitive (nickel-rich) core.[2,29,30] These include any type of gas-treated or coated CAM particles as well as particles with a nickel-deficient shell[31–33] or a nickel concentration gradient,[34,35] in which case the exposure of unprotected surfaces by cracking would be detrimental. This effect can be mitigated by tailor-made coatings or deliberate handling of CAMs, which is reported to help maintain the structure of the secondary agglomerates and to improve the cycling stability.[13,15,36,37] However, single crystalline CAMs are perhaps the most promising concept for suppressing the formation of cracks.[38,39]

In most previous studies investigating particle cracking, the electrodes had to be harvested from the cycled cells and prepared and analyzed by Kr-BET, FIB-SEM or even TEM, which are cumbersome and not generally available methods that furthermore require a large number of repeat analyses to be statistically significant. This study aims to develop a novel diagnostic tool to quantify particle cracking upon cycling using in situ electrochemical impedance spectroscopy (EIS) with a micro-reference electrode (based on a lithiated gold wire[40]). By taking into account suitable theoretical considerations, the electrochemical capacitance can be used as a measure for the electrode's electrochemically active surface area (i.e. the electrode surface area in contact with the electrolyte), which will be monitored upon the formation of cracks in cathode active material particles. In this study, we validate this method by comparing the evolution of capacitance determined by in situ EIS with a micro-reference electrode with physical surface area measurements by krypton gas physisorption, while the cracking of the particles is verified by FIB-SEM.

*Electrochemical Society Student Member.
**Electrochemical Society Fellow.
[z]E-mail: Stefan.Oswald@tum.de

Theoretical Considerations

Constant-phase element.—Electrochemical impedance spectroscopy (EIS) provides information about physical processes in electrochemical systems, which can be investigated due to their separation by different time constants. By applying an alternating potential or current in an EIS experiment to an ideal electrode/electrolyte interface in the absence of charge transfer, one would expect a purely capacitive behavior due to the capacitance of the electrochemical double layer. This theoretical capacitor appears as a vertical line in a Nyquist plot, what is expressed in complex notation as:

$$\mathbf{Z}_C = \frac{1}{\mathrm{i}\omega C} \qquad [1]$$

Assuming that the areal capacitance (i.e. the electrochemical capacitance per surface area) is distinct, constant, and uniformly distributed for each electrode material, the absolute capacitance C is a direct measure of the surface area of an electrode (see Eq. 2), a property which can, e.g. be used to assign observed features to physical properties, such as contact resistances.[41]

$$C \propto A \qquad [2]$$

Real systems like battery electrodes do not show a purely capacitive behavior, but rather have to be described by a constant-phase element (CPE).[42,43] This is commonly explained by surface roughness or a distribution of differently sized capacitive and resistive elements along the surface of the electrode.[44–46] This type of circuit element can be mathematically described through a transformation of the physical capacitor by introducing the CPE parameter Q with units $\mathrm{F/s^{1-\alpha}}$ and the phase angle α, which is independent of frequency and does not only appear as a clockwise tilt of the vertical line, but also shifts the frequency points on the line. In complex notation, this is expressed as:

$$\mathbf{Z}_{\mathrm{CPE}} = \frac{1}{(\mathrm{i}\omega)^{\alpha} Q} \qquad [3]$$

For $\alpha = 1$, one obtains the purely imaginary impedance of the physical capacitor (i.e. Eq. 3 simplifies to Eq. 1), whereas $0 < \alpha < 1$ adds a real resistive part. For $\alpha < 1$, Q does not represent a simple capacitance,[45] but should, nevertheless, scale with the electrochemically active surface area. When using Q as a measure for the surface area of the electrode, one either obtains the Q parameter from a fit of the capacitive branch of the Nyquist plot contributed by a CPE or utilizes a reasonable approximation.

Figure 1a shows the calculated impedance response of a physical capacitor with capacitance $C = 1 \cdot 10^{-3}$ F using Eq. 1 as well as of four CPEs defined by Eq. 3 with $Q = 1 \cdot 10^{-3}\ \mathrm{F/s^{1-\alpha}}$ and phase angle $\alpha \in \{0.95,\ 0.90,\ 0.85,\ 0.80\}$. For the CPEs, it appears that the imaginary part of the impedance $\mathrm{Im}(\mathbf{Z})$ at 180 mHz (blue open circles in Fig. 1a) is largely independent of the phase angle α. Through the analysis of the imaginary part of the CPE impedance as shown in Eq. 4, it becomes obvious that the dependence of the first factor $\frac{1}{\omega^{\alpha} Q}$ in the last term of Eq. 4 on the phase angle α is minor for frequencies close to $\omega = 2\pi f = 1$, i.e. for $f \approx 159$ mHz. Furthermore, for α values close to 1, the dependence of the sine term in the second factor of Eq. 4 is also very small.

$$\begin{aligned}\mathrm{Im}(\mathbf{Z}_{\mathrm{CPE}}) &= \mathrm{Im}\left(\frac{1}{(\mathrm{i}\omega)^{\alpha} Q}\right) = \mathrm{Im}\left(\frac{1}{\omega^{\alpha} Q}\exp\left(\mathrm{i}\left(-\frac{\pi}{2}\alpha\right)\right)\right)\\ &= \frac{1}{\omega^{\alpha} Q}\mathrm{Im}\left(\cos\left(-\frac{\pi}{2}\alpha\right) + \mathrm{i}\sin\left(-\frac{\pi}{2}\alpha\right)\right)\\ &= \frac{1}{\omega^{\alpha} Q}\sin\left(-\frac{\pi}{2}\alpha\right)\end{aligned} \qquad [4]$$

For this reason, one expects that the ratio of the imaginary part of the impedance of a CPE taken at phase angles close to $\alpha = 1$ and at frequencies close to $f = 159$ mHz normalized by the imaginary part of the impedance of an ideal capacitor, i.e. $\mathrm{Im}(\mathbf{Z}_{\mathrm{CPE}})/\mathrm{Im}(\mathbf{Z}_{\mathrm{CPE}}^{\alpha=1})$, described by Eq. 5 will be close to 1.

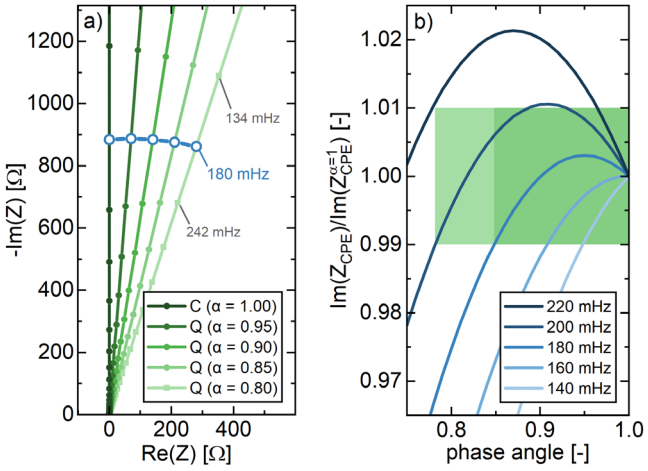

Figure 1. Simulation of constant-phase elements (CPEs) as defined in Eq. 3. (a) Nyquist plot of the impedance spectra of a pure physical capacitor ($C = 1{\cdot}10^{-3}$ F and $\alpha = 1.00$) as well as of four constant-phase elements ($Q = 1{\cdot}10^{-3}\ \mathrm{F/s^{1-\alpha}}$) with different phase angles ($\alpha \in \{0.95, 0.90, 0.85, 0.80\}$). (b) Calculation of the imaginary impedance of a CPE normalized to the imaginary part of the impedance of a capacitor, i.e. $\mathrm{Im}(\mathbf{Z}_{\mathrm{CPE}})/\mathrm{Im}(\mathbf{Z}_{\mathrm{CPE}}^{\alpha=1})$, vs. the phase angle α for different frequencies as predicted by Eq. 5. For the frequency of $f = 180$ mHz, the imaginary impedance changes less than ±1 % between phase angles of $\alpha = 1.00$ and $\alpha = 0.85$ (dark green area); for a frequency of $f = 200$ mHz, this applies for phase angles as small as $\alpha = 0.79$ (light green area). For $f = 160$ mHz, which also corresponds to $\omega = 2\pi f \approx 1\ \mathrm{s^{-1}}$, a purely sinusoidal behavior is observed.

$$\mathrm{Im}(\mathbf{Z}_{\mathrm{CPE}})/\mathrm{Im}(\mathbf{Z}_{\mathrm{CPE}}^{\alpha=1}) = -\omega^{1-\alpha} \cdot \sin\left(-\frac{\pi}{2}\alpha\right) \qquad [5]$$

This ratio of $\mathrm{Im}(\mathbf{Z}_{\mathrm{CPE}})/\mathrm{Im}(\mathbf{Z}_{\mathrm{CPE}}^{\alpha=1})$ vs. phase angle α is depicted in Fig. 1b, showing that the influence of the phase angle α on the normalized imaginary impedance is less than 1 % for $f = 180$ mHz and $\alpha > 0.85$ or for $f = 200$ mHz and $\alpha > 0.79$. For the experiments shown in this study, the impedance spectra are recorded with eight frequency points per decade, which includes the point at 180 mHz, which is why we will be focusing on this frequency point in our further discussion. From Fig. 1b it becomes obvious that the imaginary part of the impedance at a frequency of $f = 180$ mHz is, at least to a good approximation, inversely proportional to Q (see last term in Eq. 4), even if the phase angle might change during the experiment. To avoid having to fit the CPE of each impedance spectrum and having to find Q and α, we take advantage of the following approximation:

$$Q \approx \frac{1}{\omega_0 \cdot (-\mathrm{Im}(\mathbf{Z}_{\omega_0}))} \qquad [6]$$

which is within an error of ±1 % for $\omega_0 \approx 1\ \mathrm{s^{-1}}$ corresponding to a frequency of $f_0 = 180$ mHz and for $\alpha > 0.85$. Note that in this case the units of Q represent those of a capacitor (i.e. F rather than $\mathrm{F/s^{1-\alpha}}$). In the present study, we utilize this property to extract the relative change of the electrode's surface area by monitoring the change of the 180 mHz point and further compare this simplification to the exact result obtained from a fit of Q to legitimate its application experimentally. In summary, the CPE parameter Q is treated as a measure for the electrochemical capacitance, which is a good approximation at a frequency of 180 mHz and for phase angles of $\alpha > 0.85$.

Determination of surface area from impedance spectra.—In this study, we aim to use the capacitance of the electrochemical double layer of the entire composite electrode (i.e. consisting of

active material, conductive carbon, and binder) to track the cracking of active material particles due to mechanical compression or due to volume changes upon (de)lithiation. When exposed to mechanical stress, a material may develop cracks and open pores that can be penetrated by the electrolyte, thereby creating additional electrochemically active surface area. Assuming an ion radius of a lithium cation of 0.09 nm having a single-layer solvent shell of ethylene carbonate with 0.41 nm additional radius,[47] one would expect that pores larger than 1 nm in the active material can be filled by electrolyte and, therefore, be detected by probing the electrode capacitance for a given electrolyte. Any solid/electrolyte interface element of the electrode which is connected electronically through the solid part and ionically by the electrolyte thus forms an electrochemical double layer, providing a physical capacitance that can be charged or discharged similar to a physical capacitor through the displacement of ions and electrons when a potential difference is applied. In principal, this charge-transfer capacitance could be extracted from the respective *R-Q* semicircle in a Nyquist plot at any state of charge (SOC). In practice, however, the frequency range in which this charge-transfer resistance appears is similar to the ionic pore resistance, and thus these two contributions to the impedance can often not be discriminated, as discussed already by Landesfeind et al.[48] in the case of a transmission line model. However, the capacitance can be extracted separately when an electrode is in the state of quasi-infinite charge-transfer resistance, often referred to as *blocking conditions*.[49,50] For lithium-ion battery electrodes, this state is achieved either when the active material is i) fully lithiated or ii) fully delithiated or when iii) a non-intercalating electrolyte is used, whereby in all three of these cases no charge is transferred, even when a finite potential perturbation is applied.[48,51] Under these conditions, real electrode interfaces, often discussed through the Randles circuit,[42,43,52,53] then only show a purely capacitive behavior which, for low frequencies, can be described by a single constant-phase element (CPE). At these relatively low frequencies, this straight line in a Nyquist plot, in principal the onset of a huge semicircle, dominates the much smaller pore resistance and all other circuit elements, what allows the extraction of the charge-transfer capacitance from impedance spectra. Assuming a proportional relationship between capacitance and electrochemical surface area, and following the theoretical considerations discussed above, the change in surface area and, therefore, the cracking of the active material in the electrode can be monitored by electrochemical impedance spectroscopy utilizing Eq. 6.

Experimental

Electrode preparation.—NCM electrodes were prepared by mixing uncoated NCM622 ($Li_{1.01}Ni_{0.6}Co_{0.2}Mn_{0.2}O_2$, 0.3 m^2_{BET}/g, BASF SE, Germany), vapor-grown carbon fibers (VGCF-H, 12.4 m^2_{BET}/g, Showa Denko, Japan), and polyvinylidene fluoride (PVDF, Kynar HSV 900, Arkema, France) at a mass ratio of 90:8:2 with N-methyl-2-pyrrolidone (NMP, anhydrous, Sigma Aldrich, Germany) in a planetary mixer (Thinky Corp., USA) for 17 min, using a three-step sequential mixing procedure. This slurry was coated onto the rough side of an aluminum foil (18 μm, MTI, USA) with a box-type coating bar (Erichsen, Hemer, Germany) using an automated coater (RK PrintCoat Instruments, United Kingdom), and dried in a convection oven at 50 °C for 5 h. The NCM622 electrodes had a loading of 9.7 mg_{AM}/cm^2 (≡1.8 mAh/cm^2 based on 184 mAh/g_{NCM622}). The same procedure was applied for lithium titanate (LTO, $Li_4Ti_5O_{12}$, 3.0 m^2_{BET}/g, Südchemie, Germany) and lithium iron phosphate (LFP, $LiFePO_4$, LFP 400, 20.7 m^2_{BET}/g, BASF SE, Germany); however, the slurry compositions and the conductive carbon type (C65, carbon black SuperC65, 64 m^2_{BET}/g, TIMCAL, Switzerland) were adapted in accordance with Table I. Furthermore, slurries without active material, one containing only VGCF and PVDF at a mass ratio of 8:2 and one containing only C65 and PVDF at a mass ratio of 1:1 were mixed with NMP, and coatings were prepared as described above.

Electrodes with a diameter of 10.95 mm were punched out from the above prepared electrode coatings as well as from commercially available LTO electrode sheets (LTO on aluminum, 3.5 mAh/cm^2, Custom Cells, Germany). For the electrochemical cycling tests, the electrodes were used uncompressed, except for the LFP electrodes which were compressed at 200 MPa for 30 s using a KBr press (Mauthe, PE-011). For the experiments on mechanical cracking, NCM622 electrodes were compressed at 50, 100, and 200 MPa for 30 s using the KBr press. All electrodes were dried in a Büchi oven at 120 °C under dynamic vacuum for at least 6 h and then transferred to an argon-filled glove box (<1 ppm O_2 and H_2O, MBraun, Germany) without exposure to air.

Cell assembly.—The experiments on mechanical cracking were conducted in symmetric cells with NCM622 electrodes (uncompressed as well as compressed at 50, 100, and 200 MPa) and with pure VGCF electrodes, which were assembled in spring-compressed T-cells (Swagelok, USA), using two glass fiber separators (glass microfiber filter, 691, VWR, Germany) and 60 μl of non-intercalating electrolyte[51] (10 mM TBATFSI in EC:EMC 3:7 w/w).

In preparation for the cycling experiments with NCM and LFP, capacitively oversized LTO electrodes (3.5 mAh/cm^2) are used as the counter electrode, which were pre-lithiated in spring-compressed T-cells using two glass fiber separators and 60 μl LP57 (1 M $LiPF_6$ in EC:EMC 3:7 w/w, <20 ppm H_2O, BASF, Germany) against metallic lithium (450 μm thick and 11 mm in diameter, Rockwood

Table I. Overview of the properties of the electrodes prepared and investigated in this study. The composition is stated as a mass ratio of active material (AM), conductive carbon (CC), and binder (B); also provided are the areal mass loadings of the electrode and the AM, together with the thickness of the final electrode (numbers in parenthesis refer to electrodes compressed at 200 MPa), and the Kr-BET areas are also specified. Further, the specific current values are listed which are taken to define a C-rate of 1 h^{-1} as well as the upper/lower cutoff potentials and the potential at which potential-controlled EIS data (PEIS) are acquired (all referenced vs. Li^+/Li, based on an LTO counter electrode potential of 1.55 V vs. Li^+/Li), latter corresponding to 0 %SOC.

		Electrode material						
	Units	NCM622 (3.9 V)	NCM622 (4.2 V)	NCM622 (4.5 V)	LTO	LFP	VGCF only	C65 only
Composition AM:CC:B	wt%	90:8:2	90:8:2	90:8:2	90:5:5	93:4:3	0:80:20	0:10:10
Conductive carbon	—	VGCF	VGCF	VGCF	C65	C65	VGCF	C65
Areal electrode loading	$mg_{electrode}/cm^2$	10.8	10.8	10.8	10.3	13.9	1.1	0.9
Areal AM loading	mg_{AM}/cm^2	9.7	9.7	9.7	9.3	12.9	—	—
Electrode thickness	μm	~55 (~37)	~55 (~37)	~55 (~37)	~60	~116 (~75)	~40	~28
Active material BET	m^2/g_{AM}	0.3	0.3	0.3	3	20.7	—	—
Specific current @1C	mA/g_{AM}	184	184	184	170	150	—	—
Upper cutoff potential	V vs. Li^+/Li	3.90	4.20	4.50	2.05	3.80	—	—
Lower cutoff potential	V vs. Li^+/Li	2.55	2.55	2.55	1.05	2.95	—	—
Potential for PEIS	V vs. Li^+/Li	2.55	2.55	2.55	2.55	2.55	—	—

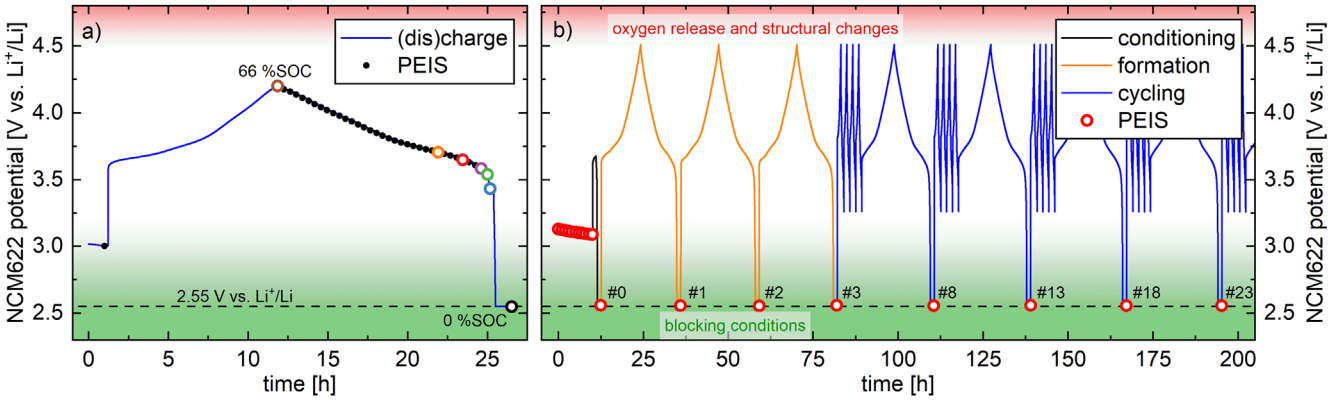

Figure 2. Cycling procedure shown exemplarily for an NCM622 working electrode in a pseudo full-cell with a pre-lithiated, capacitively oversized LTO as the counter electrode and a gold-wire reference electrode, whereby all potentials are shown vs. Li^+/Li (analogous procedures were used for LTO and LFP working electrodes). (a) Realization of blocking conditions by discharging the NCM622 working electrode to 2.55 V vs. Li^+/Li, holding it there for 1 h, and then conducting a PEIS at this potential (the colored open circles mark the potentials at which the EIS spectra shown in Fig. 4 were recorded). (b) Long-term cycling procedure, with an initial OCV phase of 10 h, a conditioning step (black line), three formation cycles (yellow lines), and cycling (blue lines). This is shown exemplarily for an NCM622 working electrode with an upper cutoff of 4.5 V vs. Li^+/Li, with the intermittent acquisition of EIS spectra (red circles), under blocking conditions at the points marked with #0, #1, etc.

Lithium, USA) to ~30 %SOC at a specific current of 15 mA/g_{AM} for 3 h, after having performed one full formation cycle at 15 mA/g_{AM}. For experiments with LTO as working electrode, pre-lithiated, capacitively oversized LTO counter electrodes were prepared using an equivalent procedure with a final charge to ~90 %SOC (corresponding to a lithium reservoir of ~3.15 mAh/cm^2) by charging for 9 h. After pre-lithiation, the LTO electrodes were harvested from the cells and used as the counter electrode in the pseudo full-cells for the electrochemical cycling tests (note that pseudo full-cell here refers to a cell with a specific working electrode and a pre-lithiated, capacitively oversized LTO electrode). The pre-lithiated, capacitively oversized LTO provides a stable half-cell potential of 1.55 V vs. Li^+/Li over a wide SOC window, a sufficiently large capacity to take up the lithium from the investigated NCM and LFP working electrodes or to provide the lithium for LTO working electrodes, and an excess of lithium compensating any lost lithium due to side reactions during cycling in order to fully (de)lithiate the working electrodes for the EIS measurements (i.e. for bringing the working electrodes into blocking conditions).

For the electrochemical cycling tests, spring-compressed T-cells with pre-lithiated, capacitively oversized LTO as the counter electrode and NCM, LFP, or LTO as working electrodes were assembled using two glass fiber separators and 60 µl LP57. Between the two separators, a micro-reference electrode (µ-RE) was installed, namely the gold-wire reference electrode (GWRE) based on the setup described by Solchenbach et al.,[40] whereby the GWRE was lithiated in situ at 150 nA over 1 h from the LTO counter electrode before cycling (note that the GWRE lithiation charge of ~0.15 µAh is negligible compared to the capacity of the counter electrode). This establishes a constant GWRE potential of 0.31 V vs. Li^+/Li,[40] which remained stable for more than 1200 h. For details about the cell setup and the preparation of the gold wire, please refer to the original publication.

To identify the specific capacitance contributed by only VGCF and PVDF or by only C65 and PVDF, the identical pseudo full-cell setup with pre-lithiated, capacitively oversized LTO (~30 %SOC) as counter electrode, two glass fiber separators, µ-RE (i.e. a GWRE) and 60 µl LP57 electrolyte was used with the respective VGCF or C65 electrodes as working electrode.

Impedance spectroscopy.—All electrochemical impedance spectra were included directly into the cycling procedure of a multi-channel potentiostat VMP3 (BioLogic, France) and recorded in a climate chamber (Binder, Germany) at 25 °C in potentiostatic mode (PEIS), with an amplitude of 15 mV for 8 points per decade from 100 kHz to 100 mHz. This results in an acquisition time of ~10 min per PEIS. Each EIS spectrum consists of a full-cell spectrum (between working and counter electrode) and, by using a GWRE, also of the half-cell spectrum (i.e. between the working and the micro-reference electrode), including a frequency point at 180 mHz. In the case of symmetric cell measurements, impedance spectra were recorded 10 h after cell assembly.

Cell testing.—All electrochemical cycling tests were performed in a climate chamber (Binder, Germany) at 25 °C, using a multi-channel potentiostat (Biologic VMP3). Before cell cycling, the GWRE was lithiated using the LTO counter electrode (see above). To acquire EIS spectra under blocking conditions, represented by a semi-infinite charge-transfer resistance, the working electrode is cycled to a state of charge of 0 %SOC at a potential of 2.55 V vs. Li^+/Li for all active materials as indicated in the last line of Table I, i.e. to either full lithiation for LFP and NCM or to full delithiation for LTO working electrodes, where the working electrode was then held for 1 h prior to taking EIS spectra. This is illustrated in Fig. 2a for an NCM622 working electrode. After an initial OCV phase of 10 h, PEIS was measured at OCV (marked by the first black circle in Fig. 2a), followed by a C/10 charge (≡18.4 mA/g_{NCM} for NCM622) in constant current (CC) mode to the upper cutoff potential (4.2 V vs. Li^+/Li in this case). At this point, where the nominal state of charge if referenced to the theoretical capacity of NCM622 (≡276.5 mAh/g_{NCM}) is 66 %SOC, another PEIS was measured (see open red circle in Fig. 2a). Subsequently, the C/10 discharge in CC mode was continued in 10 min segments with a PEIS taken at the end of each segment, which was repeated until the lower cutoff potential (2.55 V vs. Li^+/Li for NCM622) was reached, which was defined as 0 %SOC. There, a constant voltage (CV) hold of 1 h was performed, followed by a final PEIS. The procedure was executed in a similar manner for LFP and LTO, using the cutoff potentials listed in Table I. However, since LTO is delithiated in its pristine state and cell cycling of LTO starts by lithiation, the charge to the upper and the discharge to the lower cutoff potential are switched for LTO in the above given description of the cycling procedure.

To investigate the specific capacitance of the pristine materials at different potentials, the same electrode setup as described above was assembled using NCM electrodes as working electrodes as well as setups using working electrodes comprising only VGCF and PVDF or comprising only C65 and PVDF. After an initial PEIS at OCV (at ~3.0 V vs. Li^+/Li for NCM622 and at ~2.8 V vs. Li^+/Li for VGCF working electrodes) and a first OCV phase of 1 h followed by

another PEIS measurement, the potential was held for 1 h at 2.85, 2.75, 2.65, and 2.55 V vs. Li^+/Li for NCM and at 3.05, 2.95, 2.85, 2.75, 2.65, and 2.55 V vs. Li^+/Li for VGCF and C65 electrodes, including a PEIS at the respective potentials.

The long-term cycling procedure shown exemplarily for an NCM622 working electrode in Fig. 2b was initiated by an OCV phase of 10 h, during which a PEIS was taken every 1 h (red open circles in Fig. 2b). During *conditioning* (black line in Fig. 2b), the electrodes were charged at C/10 ($\equiv$18.4 mA/g_{NCM} for NCM622) in CC mode for 1 h, then discharged to the lower cutoff potential of 2.55 V vs. Li^+/Li at C/10 in CC mode, where a CV hold of 1 h was performed, followed by a PEIS. Since nickel-rich CAMs are commonly slightly overlithiated (by up to 1 %) in the synthesis process, the conditioning step was included in the procedure to ensure comparable impedance spectra for each cycle, namely by assuring that similar SOCs are obtained by the potential hold of 1 h at 2.55 V vs. Li^+/Li, especially when using different NCM active materials. For the *formation* (yellow lines in Fig. 2b), three charge/discharge cycles are executed, with a charge to the upper cutoff potential at C/10 with a CV hold until the current dropped to below 0.1 mA ($\sim$C/20, CCCV mode), and with a discharge to the lower cutoff potential at C/10 with a final CV hold of 1 h before a PEIS was recorded (marked by the #1, #2, and #3 points in Fig. 2b). The formation was followed by *cycling* (blue lines) four times at 1C ($\equiv$184 mA/g_{NCM} for NCM622) in CCCV mode in charge, until the current dropped to 0.1 mA ($\sim$C/20), and at 1C in CC mode for the discharge. The fifth cycle was performed at C/10, identical to the formation cycles, followed by a 1 h CV hold at the lower cutoff potential and a PEIS. This set of five cycles was repeated for more than 200 charge/discharge cycles. The impedance spectra taken in blocking conditions are numbered by the number of full cycles that the electrodes had performed up to that point (e.g. #8 after the first set of the five blue cycles shown in Fig. 2b). Since LTO is delithiated in its pristine state, the charge to the upper and the discharge to the lower cutoff potential are switched for LTO in the description of the cycling procedure.

For the visual investigation by FIB-SEM, additional NCM622 cells were stopped after 0.5, 1.0, and 203.5 cycles to 4.2 V vs. Li^+/Li, including a potential hold at the respective target potential, namely 4.2 V vs. Li^+/Li for non-integer cycle numbers or 2.55 V vs. Li^+/Li for integer ones.

Cell disassembly.—After cycling, the electrodes were harvested from the cells for the krypton gas physisorption measurements to determine their specific surface area and for FIB-SEM analysis. Any residue of the conductive salt was removed from the electrodes in a three-step sequential washing procedure: first, they were washed for 5 min in 5 ml EC:EMC 3:7 w/w, followed by a soaking step of 24 h in 1 ml DMC, and, finally, a washing step of 5 min in 5 ml DMC.

Scanning electron microscopy.—The morphology of fresh, mechanically compressed electrodes as well as of the ones harvested and washed after charge/discharge cycling for 0.5, 1.0, and 203.5 cycles was investigated by FIB-SEM at BASF SE (Ludwigshafen, Germany), where the electrodes were cut by focused argon-ion beam (FIB) milling and their cross-sections were investigated by scanning electron microscopy (SEM) in backscattering mode at 10 kV.

Surface area analysis.—The surface area of the harvested and washed electrodes as well as of the compressed NCM622 electrodes was determined by krypton gas physisorption at 77 K, as previously presented by Friedrich et al.,[26] measuring isothermally at 13 points between $0.01 \leqslant p/p_0 \leqslant 0.30$, using an autosorb iQ (Quantachrome Instruments, USA). Comparative N_2-BET measurements for the pristine materials (VGCF, C65, and NCM622) are within ±10 % of the specific surface areas obtained by krypton physisorption. The advantage of the measurement with krypton is a superior sensitivity of this method, since only ca. 1/100 of the total surface area is required for the physisorption measurements, so that Kr-BET areas can be obtained for 11 mm diameter electrodes, what would not be possible using N_2-BET. Prior to Kr-BET measurements, both powder samples as well as samples of pristine or harvested and washed electrodes were dried at 120 °C under vacuum for 6 h.

Results and Discussion

Mechanical compression of NCM622.—In the following, the effects of mechanical compression on NCM622 particle cracking and on the electrochemically accessible surface area or the surface area accessible by krypton gas physisorption are investigated and discussed. Figure 3a shows the cross-sectional view of an uncompressed pristine NCM622 electrode recorded by FIB-SEM. The spherical shape of the secondary agglomerates (with $\sim$5–10 μm diameter) that are comprised of numerous primary crystallites ($\sim$0.1–0.5 μm) is intact for all shown particles, which is representative of the entire electrode. Void volumes in the core of the NCM particles result from the synthesis and are observed for all cross sections through the particle centers. In contrast, Fig. 3b illustrates the compression-induced breakage of the NCM secondary particles. The applied compression of 200 MPa does not only decrease the electrode porosity from 55 % to 27 % (reflected by a decrease in electrode thickness, see Table I), but is sufficient to break the mechanically fragile secondary agglomerates into many fragments or even into single primary particles. Similar behavior has been observed for calendered battery electrodes by electron microscopy[28] as well as by X-ray tomography.[54] Due to this breakage, additional NCM surface area is exposed for compressed electrodes as compared to the uncompressed material, which is accessible for krypton gas in Kr-BET measurements as well as for the electrolyte in battery cells.

Figure 3c depicts the impedance spectra of the symmetric cells assembled with VGCF electrodes as well as with NCM electrodes that were uncompressed or compressed at 50 MPa, 100 MPa, or 200 MPa, using non-intercalating 10 mM TBATFSI electrolyte. (Note that the difference in the specific high-frequency resistance (in $\Omega \cdot g_{electrode}$) of NCM electrodes (10.8 mg/ cm^2) and VGCF electrodes (1.1 mg/ cm^2) results from the normalization to the mass of the electrodes; the absolute high-frequency resistance of $\sim$130 Ω is similar for all cells and electrodes and is typical for the 10 mM TBATFSI electrolyte with a low conductivity of $\sim$300 μS/cm). For low frequencies, all materials show purely capacitive behavior, even the NCM622 electrodes, as their charge-transfer reaction is impeded by the electrolyte with non-intercalating ions.[51] It is observed that the absolute value of the imaginary impedance at the lowest frequency of 100 mHz decreases with increasing compression of the NCM electrodes. The same can be observed for the absolute value of the imaginary impedance of the 180 mHz point (open circles in Fig. 3c), which decreases from 16.6 $\Omega \cdot g_{electrode}$ for the uncompressed NCM622 electrodes to 14.5 $\Omega \cdot g_{electrode}$ for a compression of 50 MPa, further to 11.9 $\Omega \cdot g_{electrode}$ for 100 MPa, and even to 10.4 $\Omega \cdot g_{electrode}$ for 200 MPa. Since a decrease of the absolute value of the imaginary low-frequency impedance of a CPE element corresponds to an increase of its capacitance parameter Q (see Eq. 3), a compression of the NCM622 particles results in an increase in their capacitance. We assign this increase in capacitance to an increase in electrochemically active surface area of the NCM622 particles in the entire electrode, which would actually be expected based on the observed NCM622 particle breakage upon compression (see Fig. 3b). By fitting the capacitive branch between 100 mHz and 1 Hz with an *R-Q* element, the CPE parameter Q and the phase angle α can be determined, whereby the values of latter are noted in Fig. 3c. The decrease of α with increasing compression from 0.87 to 0.84 (visible by a clockwise tilt of the capacitive branch) is most likely related to the reduced relative contribution of the CPE with a very high value of $\alpha = 0.97$ that is characteristic of the VGCF carbon fibers to the total CPE as the NCM622 surface area increases. However, since the obtained values of α are close to or larger than

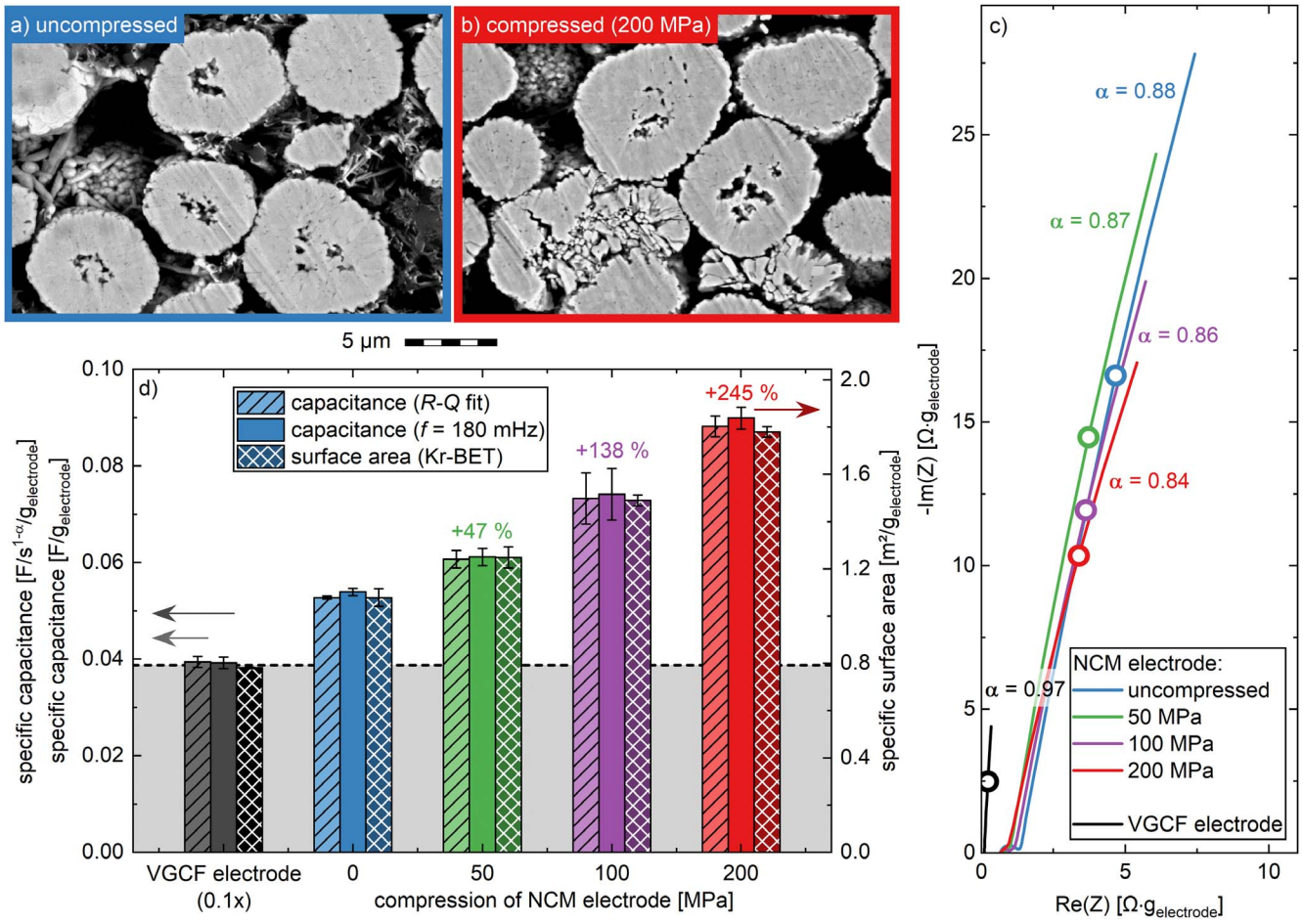

Figure 3. Effect of mechanical compression on pristine NCM622 electrodes: cross-sectional view by FIB-SEM in backscattering mode at 10 kV: (a) uncompressed electrode and (b) electrode compressed at 200 MPa. (c) Nyquist plots of symmetric cells at 25 °C with VGCF electrodes and with pristine NCM622 electrodes that were uncompressed or compressed at 50, 100, or 200 MPa, all assembled with 60 µl of 10 mM TBATFSI. The values for the phase angle α obtained from the fit of the capacitive branch by an *R-Q* element between 100 mHz and 1 Hz are listed in the figure, and the frequency points at 180 mHz are indicated by larger empty circles. (d) The left *y*-axis shows the specific capacitance extracted from the impedance spectra of the symmetric cells depicted in (c), either via a fit with an *R-Q* element between 100 mHz and 1 Hz (hatched bars) or via the imaginary impedance at 180 mHz according to Eq. 6 (solid bars). The right axis shows the specific surface area determined by krypton gas physisorption of VGCF electrodes and of pristine NCM622 electrodes that were uncompressed or compressed at 50, 100, or 200 MPa (cross-hatched bars). Note that the specific capacitance and the specific surface area for the VGCF electrode were divided by 10, accounting for the fact that 1 g of an NCM electrode contains 0.08 g VGCF and 0.02 g PVDF, which corresponds to that in 0.1 g of a VGCF electrode. The thus estimated capacitance and specific surface increase of the NM622 particles in the NCM622 electrodes (in %) is marked above each set of bars. The values shown here are calculated from the mean of two identical cell pairs for PEIS or of two electrodes for BET, and the error bars correspond to the minimum/maximum value of two measurements.

0.85, the assumptions used for Eq. 6 still apply, so that the approximate capacitance of the electrode can be obtained from the imaginary part of the impedance at 180 mHz.

In Fig. 3d, we compare the compression-induced increase of the specific capacitance $Q/m_{electrode}$ (left axis) of the NCM622 electrodes, extracted from the fit of the capacitive branch (hatched bars) or from the imaginary part of the impedance at 180 mHz via Eq. 6 (solid bars), with that of the increase of the specific surface area obtained by krypton gas physisorption (cross-hatched bars, plotted against the right axis). The specific capacitance of the pristine NCM622 electrode of 0.053 $F/s^{1-\alpha}/g_{electrode}$ increases by 15 % when it is compressed at 50 MPa, by 39 % at 100 MPa, and by even 67 % at 200 MPa (hatched bars in Fig. 3d). When the capacitance is not extracted from an *R-Q* fit, but simply through the imaginary value of the impedance at the 180 mHz point using Eq. 6 (see solid bars in Fig. 3d, plotted against the left axis), the obtained results (now in units of $F/g_{electrode}$) are essentially identical to the numerical *Q*-values extracted from the *R-Q* element fit, which experimentally proves the validity of the theoretical assumptions of this simplified method. To determine the relative change of the capacitance of only the NCM622 particles upon compression, the capacitance contribution from the conductive carbon and binder must be subtracted. This contribution is measured through the same setup, using VGCF electrodes, yielding 0.394 $F/s^{1-\alpha}/g_{electrode}$ or 0.392 $F/g_{electrode}$ using Eq. 6. Since 1 g of the NCM622 electrode comprises 0.08 g of VGCF and 0.02 g of PVDF (see Table I), the capacitance contribution of the VGCF/binder composite in 1 g NCM622 electrode corresponds to 1/10 of that of the mass normalized capacitance of the VGCF electrode, i.e. 0.0394 $F/s^{1-\alpha}/g_{electrode}$, which is marked by the black hatched bar in Fig. 3d (or 0.0392 $F/g_{electrode}$ using Eq. 6, marked by the black solid bar). Assuming that the capacitance contribution of VGCF and PVDF in the NCM622 electrode is the same as that in the VGCF electrode, the capacitance contributed by the NCM622 particles in the NMC622 electrodes is the total capacitance of the NCM622 electrode minus 1/10 of the capacitance of the VGCF electrode, indicated by the capacitance extending beyond the black dashed horizontal line in Fig. 3d. Thus, if the capacitance increase of the NCM622 electrodes with compression is

referenced to the estimated NCM622 contribution, it increases by 47 %, 138 %, and 245 %, when compressing the NCM622 electrodes at 50, 100, and 200 MPa, respectively.

To prove that this increase in capacitance upon mechanical compression is proportional to the increase in the specific surface area of the electrodes and of the NCM622 particles in the electrodes, the specific surface area of the NCM622 electrodes was quantified by krypton BET. The Kr-BET surface area increases from 1.08 $m^2/g_{electrode}$ of the uncompressed NMC622 electrode by 16 %, 38 %, and 65 % for a compression of 50, 100, and 200 MPa, respectively (cross-hatched bars in Fig. 3d). This increase in the total specific surface area is within the error bars in perfect agreement with the observed increase in the total capacitance obtained by the impedance measurements (namely 15 %, 39 %, and 67 % for a compression of 50, 100, and 200 MPa, respectively). This not only proves that the increase in capacitance is indeed related to an increase in specific surface area (something one would anyways expect), but also the validity of the approximation that the Q parameter of the CPE response of the electrode (in units of $F/s^{1-\alpha}/g_{electrode}$) can be equated with the capacitance of the electrode (in units $F/g_{electrode}$), at least as long as the α-value is sufficiently large. Furthermore, it indicates that the estimation of the capacitance through the 180 mHz point is sufficiently accurate and is a valid approximation for the experiments conducted in this study.

Using the Kr-BET analysis, we can now examine whether the above estimate of the capacitance contribution by the NCM622 particles is valid. For this, we measured the Kr-BET area of the VGCF electrode (7.8 $m^2/g_{electrode}$), which is ~20 % smaller than the predicted value of 9.9 $m^2/g_{electrode}$ based on the 12.4 $m^2/g_{electrode}$ for the pristine VGCF fibers and the 80 wt% VGCF content in the VGCF electrodes. (Note that the same was observed when comparing BET areas of several carbon blacks with that of electrodes made of carbon black and Nafion® binder, which was ascribed by partial pore blocking by the binder.[55]) By multiplying the VGCF electrode Kr-BET area by 0.1 (as explained above), the estimated Kr-BET area contribution from the VGCF/PVDF components to the NCM622 electrode would be 0.78 $m^2/g_{electrode}$ (black cross-hatched bar in Fig. 3d). Thus, the specific surface area measured for the NCM622 electrodes which extends above this value (black dashed line in Fig. 3d) would have to be equal to the specific surface area contributed by the pristine NCM622 particles. For the uncompressed NCM622 electrodes, the difference in specific surface area between the estimated contribution by the VGCF/PVDF components (0.78 $m^2/g_{electrode}$) and the one measured for the NCM622 electrode (1.08 $m^2/g_{electrode}$) equates to 0.30 $m^2/g_{electrode}$, which is identical with the BET surface area of the pristine NCM622 particles. This clearly proves our above assumption that the specific surface area and the capacitance contributions from the VGCF/binder components of the NCM622 electrode can be simply subtracted by using the mass-fraction corrected specific capacitances and specific surface areas of pure VCGF electrodes, thereby yielding the desired values for the specific surface area and the specific capacitance contributed solely by the NCM622 particles in the NCM622 electrodes.

Realization of blocking conditions for NCMs.—When cycling battery cells using a conventional electrolyte containing intercalating ions (a non-blocking electrolyte so to speak), blocking conditions that represent a state of quasi-infinite charge-transfer resistance can be achieved by either fully lithiating or fully delithiating the active material during the charge/discharge procedure. Since NCM materials become unstable and degrade significantly at high SOC,[5,56] NCMs cannot be fully delithiated reversibly, so blocking conditions can only be achieved towards 0 %SOC when the NCM is fully lithiated. To achieve full lithiation of the working electrode at selected points during a typical charge/discharge cycling procedure, a capacitively oversized, pre-lithiated counter electrode with a stable potential is required. For this, we here use LTO; a metallic lithium counter electrode would in principle also satisfy these requirements, but its long-term cycling stability is inferior to that of pre-lithiated LTO.

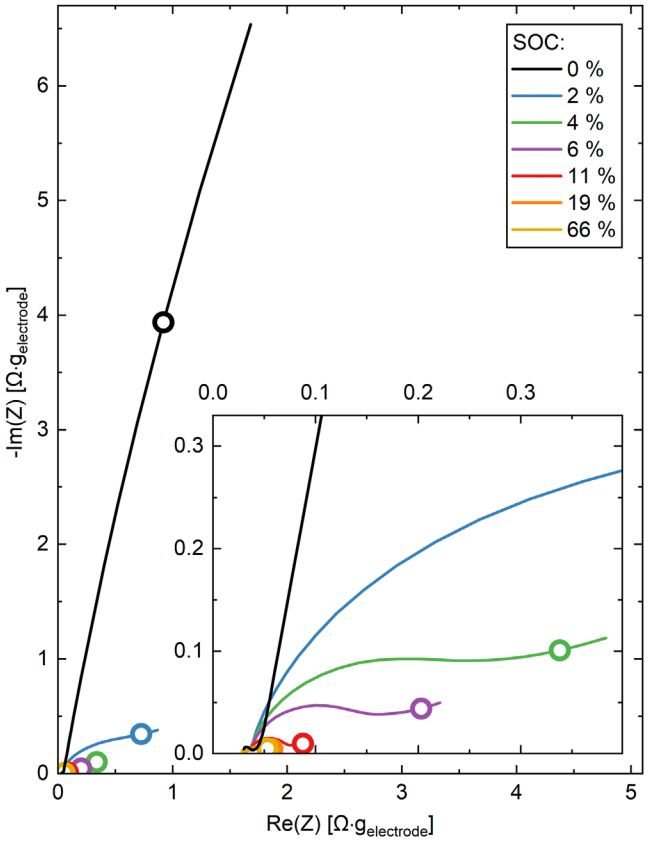

Figure 4. Realization of blocking conditions in conventional electrolyte, shown exemplarily for NCM622. For this, pseudo full-cells were assembled in Swagelok T-cells with 60 µl LP57, two glass fiber separators, and a µ-RE (i.e. a GWRE) using NCM622 as the working electrode and pre-lithiated, capacitively oversized LTO as the counter electrode. Following the procedure introduced in the experimental part and depicted in Fig. 2a, the impedance spectra of an NCM622 working electrode were recorded at 25 °C at different SOCs between 4.20 V and 2.55 V vs. Li^+/Li, applying an amplitude of 15 mV from 100 kHz to 100 mHz. Nyquist plots of selected impedance spectra show an increasing charge-transfer semicircle with decreasing SOC, developing into blocking conditions for 0 %SOC. The frequency points at 180 mHz are indicated by large open circles.

Figure 4 depicts selected impedance spectra of an NCM622 electrode as a function of its SOC, extracted from the procedure depicted in Fig. 2a and using a GWRE to exclusively monitor the impedance spectra of the working electrode.[40] At 4.2 V vs. Li^+/Li, corresponding to 66 %SOC when referenced to the theoretical NCM622 capacity of 276.5 mAh/g_{NCM}, the impedance spectrum in the Nyquist plot shows (apart from the HFR offset by the electrolyte resistance in the separator) only one relatively small semicircle of ~0.015 $\Omega \cdot g_{electrode}$ with an apex frequency of 116 Hz (see yellow line in Fig. 4) that is assigned to the NCM622 charge-transfer resistance convoluted with the ionic pore resistance.[48] Upon decreasing the SOC to 19 %SOC (orange line), the size of the semicircle remains approximately constant and only grows significantly with each lithiation step at lower SOCs, as can be seen for the data at 11 %SOC (red line). After the final potential hold at 2.55 V vs. Li^+/Li for 1 h, the semicircle is converted to a purely straight line of a CPE with $\alpha = 0.85$. At this low potential, the NCM622 active material is fully lithiated, which inhibits the charge-transfer reaction and thus increases the charge-transfer resistance to a very large, quasi-infinite value. In this state, the NCM622 active material shows only capacitive behavior, as observed for the impedance response of the NCM622 electrodes in non-intercalating electrolyte (see Fig. 3c); as the capacitive impedance response at low frequencies exceeds that of the ionic pore resistance by orders of magnitude, it can be used as

a direct measure of the electrode's surface area. By implementing a potential hold at 2.55 V vs. Li^+/Li into a charge/discharge cycling procedure with NCM cathodes, we are therefore able to monitor its capacitance from the impedance spectra in blocking conditions. As we have shown that the thus quantitively determined capacitance is proportional to the specific surface area of the NCM active material (see Fig. 3d), this approach allows to monitor the specific surface area change of NCM cathode active materials due to particle breakage over the course of charge/discharge cycling. As blocking conditions for NCMs can only be achieved at 0 %SOC, i.e. in the fully lithiated state in which the NCM unit cell volume is the largest, there is the possibility that cracks that may have formed at high SOCs (i.e. at low NCM unit cell volume) may have closed reversibly, so that the area between these cracks would not be wetted by electrolyte and not contribute to the measured capacitance. Therefore, only irreversible crack formation in the active material particles can be observed with this method utilizing blocking conditions.

Furthermore, blocking conditions could also be realized for electrodes comprising LTO or LFP, for both materials at a potential of 2.55 V vs. Li^+/Li (see Fig. S1 which is available online at stacks.iop.org/JES/167/100511/mmedia), following a procedure similar to the one used for the NCM622 electrodes. While layered oxides degrade at high SOCs and, therefore, cannot be fully delithiated to bring them into blocking conditions at 100 %SOC, other active materials, such as LFP, are stable at both ends of the SOC window, so that for these blocking conditions can be achieved at full lithiation as well as at full delithiation (shown, e.g. for $LiNi_{0.5}Mn_{1.5}O_4$[48]). For a better comparability with the pristine state, the impedance spectra were recorded in the fully lithiated state for LFP and in fully delithiated state for LTO, corresponding to 0 %SOC at 2.55 V vs. Li^+/Li for both materials.

Specific capacitance of pristine electrode constitutents.—As discussed above, to quantify the relative capacitance increase of the examined active material from the capacitance increase of the electrode, the specific capacitance of each electrode component needs to be identified. In the analysis based on symmetric cells presented in Fig. 3d, this was accomplished by subtracting the specific capacitance of the VGCF electrode from that of the NCM622 electrode. However, since the specific capacitance of a given electrode material will likely depend on both the potential and the type of electrolyte,[57] any comparative measurements and the measurements for the background correction due to the conductive carbon and the binder components must be conducted at the same potential and in the same electrolyte. For the following long-term cycling experiments with NCM622 electrodes in LP57 electrolyte, where we will conduct impedance analysis of the NCM622 working electrode in blocking conditions at 2.55 V vs. Li^+/Li, we have therefore evaluated the specific capacitance of the NCM622 and of the PVDF electrodes as a function of potential in the LP57 electrolyte (1 M $LiPF_6$ in EC:EMC 3:7 w/w), using pre-lithiated LTO as counter electrode and a µ-RE (i.e. a GWRE).

The specific capacitance of the pristine uncompressed NCM electrodes in the LP57 electrolyte at 2.55 V vs. Li^+/Li is 0.12 $F/g_{electrode}$ (based on two independent experiments; see Fig. S2), which is ~9 % higher than the value of 0.11 $F/g_{electrode}$ obtained at OCV (corresponding to ~3.0 V vs. Li^+/Li). Interestingly enough, while the latter potential should closely correspond to the NCM622 potential in the symmetric cell experiments conducted with non-intercalating electrolyte (10 mM TBATFSI in EC:EMC 3:7 w/w.), the specific capacitance we had obtained in this case is ~2-fold lower (0.054 ± 0.01 $F/g_{electrode}$, see blue solid bar in Fig. 3d). The potential dependence of the specific capacitance of the VGCF electrode in the LP57 electrolyte is similarly weak as that of the NCM622 electrode (see Fig. S2), yielding 0.43 ± 0.01 $F/g_{electrode}$ at 2.55 V vs. Li^+/Li and ~0.39 $F/g_{electrode}$ at OCV (corresponding to ~2.8 V vs. Li^+/Li); in this case, the difference to the specific capacitance obtained in symmetric cells with non-intercalating electrolyte is rather minor (0.39 $F/g_{electrode}$, see black solid bar in Fig. 3d). Due to these unpredictable but significant dependencies of the specific capacitances on potential and electrolyte type, it becomes clear that comparative measurements always must be done under identical conditions.

As commercial electrodes typically use C65 as conductive carbons (or other carbon blacks with similar BET surface area), we also examined the specific capacitance of C65 electrodes (50 wt% C65 and 50 wt% PVDF, see Table I). As one would expect due to the much higher BET area of C65 compared to VGCF fibers (64 vs. 12.4 m^2/g), the specific capacitance of C65 electrodes at 2.55 V vs. Li^+/Li amounting to 1.7 $F/g_{electrode}$ (see Fig. S2) is much higher than that of the VGCF electrodes (0.43 $F/g_{electrode}$).

Charge/discharge cycling of NCM622 electrodes.—To monitor the electromechanical NCM622 particle breakage upon cycling, the electrode must contain fully intact secondary agglomerates, i.e. NCM622 particles must not have been fractured by electrode compression before cell cycling. Based on our analysis of the effects of mechanical compression of the electrodes (see Fig. 3), this necessitates that uncompressed NCM622 electrodes are used. To ensure electronic connection throughout the entire electrode even without compression, vapor-grown carbon fibers with a length of 15 µm were used as conductive additives, rather than the commonly used C65 carbon black. As it will be shown later, the initial performance of these electrodes (for detailed composition, see Table I) is what one would expect for this NCM622 active material using C65 carbon black as conductive electrode constituent.

Prior to charge/discharge cycling, it was verified that the impedance spectra of the NCM622 working electrode are stable over time during the initial OCV phase of 10 h in order to exclude any time-dependent effect on the impedance (data not shown). Figure 5a shows three selected impedance spectra of the same NCM622 electrode after the conditioning cycle (referred to as #0), after 3 formation cycles (referred to as #3), and after 203 cycles with an upper cutoff potential of 4.2 V vs. Li^+/Li (see Fig. 2b for a sketch of the cycling procedure). First, it is observed that blocking conditions are achieved in all instances through the full lithiation of the NCM622 particles after the 1 h long potential hold at 2.55 V vs. Li^+/Li. It should be noted that the semicircle at high frequencies is due to a contact resistance, as was shown previously for uncompressed LFP[51,58] and uncompressed $LiNi_{0.5}Mn_{1.5}O_4$[41] electrodes. While the phase angle of the NCM622 electrodes during the initial OCV phase is approximately $\alpha = 0.90$ (data not shown), it decreases to $\alpha = 0.89$ after conditioning (see spectrum #0 in Fig. 5a), to $\alpha = 0.88$ after formation (see spectrum #3) and to $\alpha = 0.87$ after cycle 203 (see spectrum #203). Even for the highest upper cutoff potential of 4.5 V vs. Li^+/Li, the phase angle does not decrease below $\alpha = 0.85$ over a total of 303 test cycles (the full number of cycles are shown in Fig. S3), wherefore the theoretical considerations in the theory section still apply (see Fig. 1), so that the expected error for approximating the capacitance with the Q-value of the CPE extracted at a frequency of 180 mHz should still be below ±1 %. As illustrated by the impedance data for cells cycled to 4.2 V vs. Li^+/Li, the fact that the value of Q (or the capacitance) increases with increasing cycle number can be seen by the decreasing imaginary impedance at 180 mHz that is marked by the open by circles in Fig. 5a: it decreases from 6.90 $\Omega \cdot g_{electrode}$ after the conditioning cycle (cycle #0) to 4.94 $\Omega \cdot g_{electrode}$ after the 3 formation cycles, all the way to 3.36 $\Omega \cdot g_{electrode}$ after 203 cycles to an upper cutoff of 4.2 V vs. Li^+/Li. Based on Eq. 6, this corresponds to an increase of electrode capacitance of 40 % between cycle 0 and cycle 3, and of 109 % between cycle 0 and cycle 203.

Figure 5b shows this increase in capacitance of NCM622 electrodes, depicted as specific capacitance in units of $F/g_{electrode}$, vs. cycle number for NCM622 pseudo full-cells cycled to different upper cutoff potentials of 3.9, 4.2, and 4.5 V vs. Li^+/Li. For comparison, the specific capacitance of the pristine NCM622 electrode of 0.12 ± 0.00 $F/g_{electrode}$ (see Fig. S2) is marked by the two gray

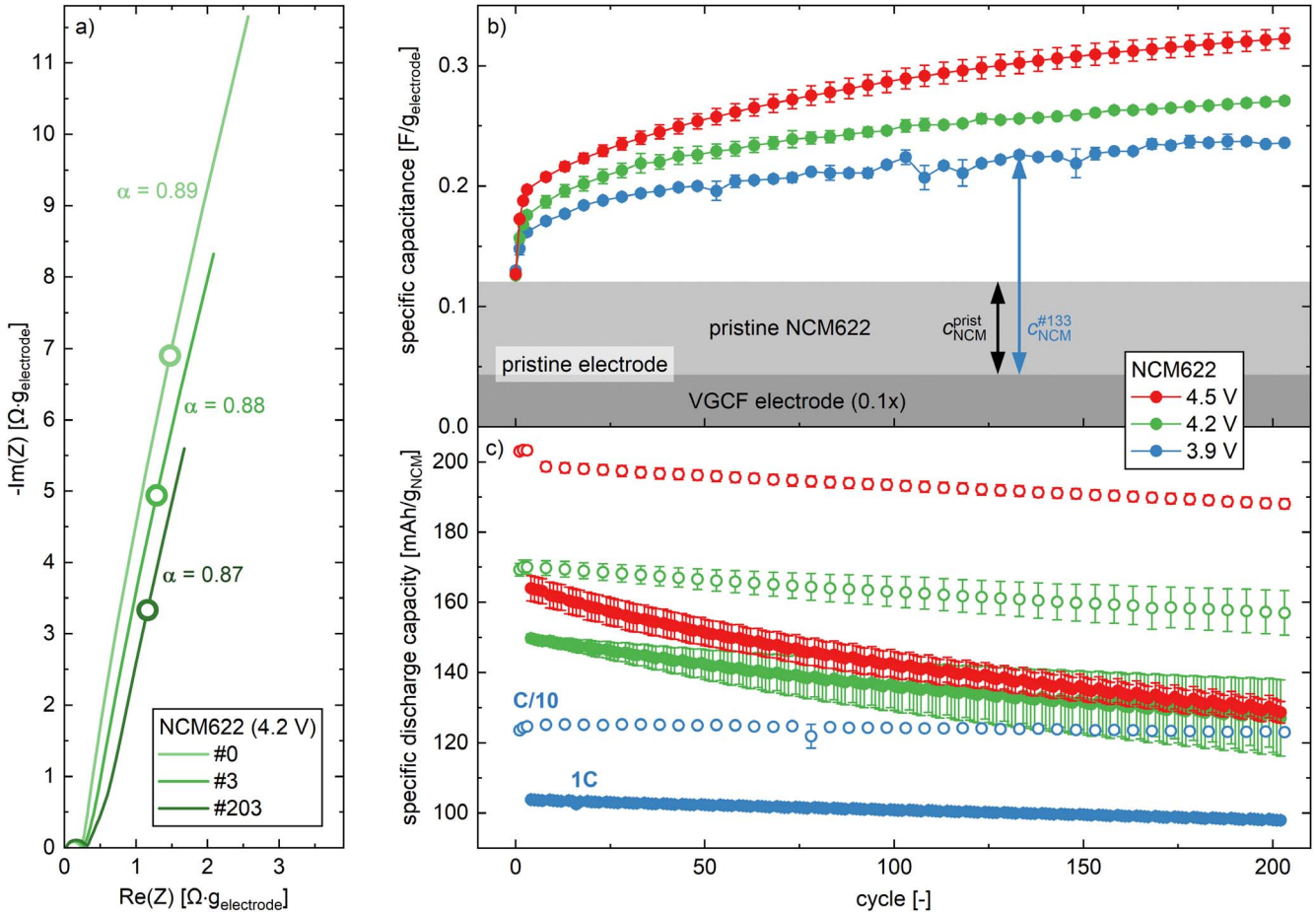

Figure 5. Electrochemical cycling of NCM622 in pseudo full-cells with 60 µl LP57, two glass fiber separators, and a µ-RE (i.e. a GWRE) using an uncompressed NCM622 working electrode and pre-lithiated, capacitively oversized LTO as the counter electrode. Following the procedure depicted in Fig. 2b, NCM622 was cycled at 25 °C to different upper cutoff potentials of 3.9 V (blue lines/symbols), 4.2 V (green lines/symbols), or 4.5 V (red lines/symbols) vs. Li^+/Li. Impedance spectra of the NCM622 working electrodes were recorded in blocking conditions after a potential hold at 2.55 V vs. Li^+/Li, applying an amplitude of 15 mV from 100 kHz to 100 mHz. The specific capacitance and the specific discharge capacity values shown here are calculated from the mean of two nominally identical cells, with the error bars corresponding to the minimum/maximum value of two cells. (a) Selected impedance spectra in blocking conditions of the NCM622 working electrode after the conditioning cycle (referred to as #0), after three formation cycles (referred to as #3), and after 203 cycles (referred to as #203) to an upper cutoff potential of 4.2 V vs. Li^+/Li (see also Fig. 2b). (b) Specific capacitance of the NCM622 working electrode extracted from the imaginary impedance at a frequency of 180 mHz in blocking conditions (see Eq. 6). The sum of the gray areas indicates the specific capacitance of the pristine uncompressed NCM622 working electrode, and the dark gray area shows the specific capacitance of a VGCF electrode multiplied by 0.1 (see text). (c) Specific discharge capacity normalized to the active material mass vs. cycle number following the procedure shown in Fig. 2b. The open circles show the discharge capacity at C/10 (after a CCCV charge at C/10), and the solid circles at 1C (after a CCCV charge at 1C).

colored areas. By subtracting 1/10 of the specific capacitance of a VGCF electrode which equates to 0.043 ± 0.01 $F/g_{electrode}$ (analogous to what was done when constructing Fig. 3d), indicated by the dark gray colored area in Fig. 5b, the capacitance contributed solely by the NCM622 active material is obtained (i.e. the light gray area). Furthermore, since it is assumed to be proportional to the surface area of the NCM622 active material, the relative increase of the surface area of the NCM622 particles with cycling should be proportional to the ratio of the thus estimated NCM622 capacitance at any given cycle number (marked by the blue arrow in Fig. 5b for cycle #133) and the NCM622 capacitance prior to cycling (marked by the black arrow).

After conditioning (cycle #0), the specific capacitance of the NCM electrodes is increased by ∼6 % compared to the pristine electrodes (marked by the light gray area). Since the unit cell volume change for this very small SOC change of 7.5 % (referenced to 276.5 mAh/g_{NCM}) is rather negligible ($\Delta V/V \approx -0.3$ %),[7] cracking of the NCM622 particles is not expected. Nevertheless, this small volume change seems to already be sufficient to increase the specific capacitance of the electrode, which we interpret to be caused by the formation of a small extent of irreversible cracks in the NCM particles. This cracking at very small volume changes may be related to the fact that these NCM622 particles are not monocrystalline, but consist of thousands of primary particles, which may decrease the stability of the material upon even very small unit cell volume changes. For all three upper cutoff potentials, the major portion of the increase in specific capacitance (i.e. of surface area increase, presumably via crack formation) occurs during the first few cycles. For example, after the first three formation cycles an upper cutoff potential of 4.2V (green symbols), the NCM622 electrode capacitance increases by 47 % compared to the pristine electrode, and ultimately increases by 125 % after 203 cycles. The fact that the largest capacitance increase per cycle occurs over the first few cycles suggests that the crack formation due to the unit cell volume changes upon repeated (de)lithiation is most pronounced during the first cycles, until a major part of the mechanical stress is dissipated at the mechanically weakest interfaces and, therefore, a reduced rate of capacitance increase (i.e. a reduced crack formation rate) is observed for later cycles. After roughly 30 cycles, a continuous increase of the capacitance is observed for the three different cutoff potentials. This may not only be related to mechanical crack formation, but may also be caused by the chemical decomposition of Li_2CO_3, LiOH, and

Li_2O residuals remaining after the synthesis of the NCM622 active material, which might be decomposed chemically by protic species released upon cycling,[59] creating pores between the primary crystallites that also contribute to the continuous capacitance and surface area increase. In general, Fig. 5b shows that the capacitance increase is larger for higher cutoff potentials, as one might expect due to the associated larger unit cell volume changes (see below discussion). Based on these observations, we hypothesize that the unit cell volume changes upon (de)lithiation induce particle cracking and a concomitant increase in surface area, which is reflected by the increasing capacitance upon cycling.

Figure 5c shows the discharge capacities vs. cycle number for these NCM622 electrodes, from which one can examine how particle breakage might impact its cycling stability. As these tests were conducted with pre-lithiated, capacitively oversized LTO counter electrodes with a large lithium reservoir, capacity fading due to the loss of active lithium can be excluded. The open circles show the discharge capacity of the C/10 cycles ($\equiv$18.4 mA/g_{NCM}) conducted prior to each PEIS measurement in blocking conditions (every 5th cycle, see Fig. 2b), while the solid circles show the four 1C cycles conducted in between the PEIS measurements. The initial performance of these NCM622 electrodes with VGCF conductive carbon is reasonably close to what is reported for conventional NCM622 electrodes (i.e. with C65 conductive binder): at the upper cutoff potential of 4.5 V vs. Li^+/Li, the here obtained initial capacity of $\sim$204 mAh/g_{NCM} at C/10 and of $\sim$165 mAh/g_{NCM} at 1C (see red symbols in Fig. 5c) is comparable to the initial specific capacities of $\sim$195 mAh/g_{NCM} at C/10 and the $\sim$175 mAh/g_{NCM} at 1C reported by Jung et al.[60] (the latter cells were cycled against graphite, whereby 4.4 V vs. graphite correspond to roughly 4.5 V vs. Li^+/Li).

At C/10 and at the lowest cutoff potential of 3.9 V vs. Li^+/Li, the capacity remains at 124 mAh/g_{NCM} for more than 200 cycles (blue open symbols in Fig. 5c). As the upper cutoff potential is increased to 4.2 or 4.5 V, a constant fading of the discharge capacity is observed over the 203 cycles, starting from the very first cycle: at 4.2 V from initially 169 to 157 mAh/g_{NCM} after 203 cycles (−7 %), and at 4.5 V from initially 204 to 188 mAh/g_{NCM} after 203 cycles (−8 %). Since the counter electrode provides an excess of cyclable lithium, and since overpotentials are relatively small at such a slow C-rate, the here observed capacity fading at C/10 must be related to an enhanced extent of particle breakage for these higher cutoff potentials, which we believe leads to a loss of the electronic connection to some fragments of the NCM622 active material. This furthermore suggests that the relatively small unit cell volume change of −1.0 % for an upper cutoff potential of 3.9 V and the associated particle cracking that is indicated by the capacitance increase (see Fig. 5b) is not sufficient to totally disconnect the NCM622 active material particles, otherwise some capacity fading would be observed.

At the higher rate of 1C, the capacity fading for a cutoff potential of 3.9 V vs. Li^+/Li is rather minor, from 104 mAh/g_{NCM} at the beginning of test to 98 mAh/g_{NCM} after 203 cycles (−6 %). Since in this case capacity fading is only noted at the higher rate of 1C, we assign this effect to an increased overpotential due to a poor electronic connectivity between the fragments of the cracked secondary NCM622 agglomerates, yet without a complete electronic isolation. Much higher capacity fading is observed for 4.2 V upper cutoff potential, namely from 150 to 127 mAh/g_{NCM} (−15 %) over the same number of cycles, which we again ascribe to a poor electronic connectivity within the NCM622 secondary agglomerate due to more extensive cracking. At the highest upper cutoff potential of 4.5 V, the capacity fading at 1C is even more pronounced (from 164 to 129 mAh/g_{NCM}, corresponding to −21 %) and is approximately 3-fold higher than that at C/10 (−8 %). At such a high cutoff potential, however, the capacity fading will likely also have contributions from a rock-salt like surface layer that is formed upon lattice oxygen release, which is reported to occur at around 80 %SOC,[5] i.e. close to upper cutoff potentials of 4.5 V vs. Li^+/Li for NCM622.[60] The thus formed poorly conductive surface layer around the active material particles was suggested to increase the electronic resistance and thus the overpotential at higher C-rates.[26] The effect of oxygen release on particle cracking and capacity fading will be discussed further in Part II of this study. To conclude, we believe that the capacity fading at 3.9 V vs. Li^+/Li is solely attributed to a loss of electronic connection of some NCM622 active material fragments; at 4.2 V, some fragments become totally isolated electronically, and at 4.5 V, particle breakage and oxygen release lead to both material loss as well as resistance growth.

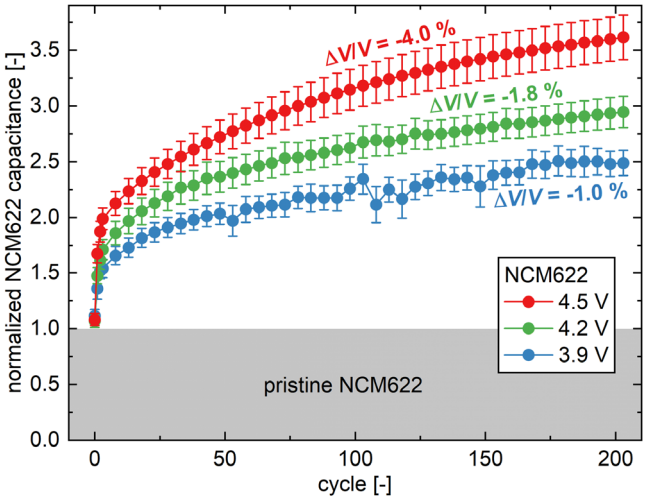

Figure 6. Capacitance contributed by the NCM622 particles in the NCM622 electrodes, normalized by their capacitance in the pristine NCM622 electrode vs. cycle number for the three upper cutoff potentials of 3.9 V (blue symbols), 4.2 V (green symbols), and 4.5 V (red symbols) vs. Li^+/Li. Data were extracted from Fig. 5, whereby the NCM622 capacitance contribution was obtained by subtracting the capacitance contribution of the VGCF electrode (dark gray area in Fig. 5b) from the overall NCM622 electrode capacitance (symbols in Fig. 5b). The error bars are determined by the laws of error propagation (see supporting information), using the average capacitances and their minimum/maximum values given by Fig. 5b. The relative volume change of the unit cell upon delithiation as measured by XRD[7,61,62] (i.e. $\Delta V/V$) for the three different upper cutoff potentials is specified in the figure.

Since the specific capacitance against cycle number described in Fig. 5b is composed of the contributions of the NCM622 active material, the conductive carbon, and the binder, we estimate the capacitance contribution from the NCM622 active material particles by subtracting the specific capacitance of the VGCF electrode in the same manner as done for the evaluation of the data in Fig. 3d. This assumes that the capacitance of the VGCF electrode can be subtracted by considering the weight fractions of the VGCF/PVDF components in the NCM622 electrode (10 wt%), and that their capacitance does not change over cycling (a reasonable assumption, as the VGCF fibers experience no ion (de)intercalation during cycling in this voltage region). Based on this, we can determine the relative change of the capacitance of the NCM622 particles over the cycling experiment (see Fig. 5a) normalized that of the pristine NCM622 particles, namely by taking the ratio of the difference of the capacitance at a given cycle and the capacitance of the VGCF electrode (illustrated by the blue arrow for cycle #133 in Fig. 5b) over this difference after the conditioning cycle (represented by the black arrow in Fig. 5b). Figure 6 shows the thus estimated normalized capacitance changes of the NCM622 particles over cycling for the three different upper cutoff potentials of 3.9 V (blue symbols), 4.2 V (green symbols), and 4.5 V (red symbols); the error bars are based on the minimum/maximum values of the measured electrode capacitances (see Fig. 5b) and the error propagation when equating capacitance differences and equating their ratio (explained in more detail in the supporting information).

Since the NCM622 particle capacitance is expected to be directly proportional to their electrochemically accessible surface area (i.e. to

the NCM622 particle area in contact with the electrolyte), the evolution of the normalized NCM622 particle capacitance shown in Fig. 6 should be directly proportional to the cracking-induced increase in the specific NCM622 surface area over the course of cycling, if a constant surface area normalized double layer capacitance is assumed. As shown in Fig. 6, the evolution of the normalized NCM622 particle capacitance and, presumably, of its electrochemically active specific surface area rapidly increases within the first three formation cycles (cycles #0 to #3) and then more gradually over the subsequent cycles, following the trend shown in Fig. 5b. This behavior coincides nicely with the results obtained by acoustic emission experiments on transition metal oxides as well as on silicon, all showing that the cracking of the active material particles appears predominantly during the first few cycles.[63–65] The total increase of the normalized NCM622 capacitance scales approximately with the relative volume change of the unit cell ($\Delta V/V$) measured through XRD,[7,61,62] and specified in Fig. 6 for the different upper cutoff potentials: (i) for 3.9 V vs. Li^+/Li, where $\Delta V/V$ during NCM622 delithiation amounts to -1.0 %, the NCM622 capacitance increased by 149 % over 203 cycles; (ii) for 4.2 V, where $\Delta V/V$ amounts to -1.8 %, the NCM 622 capacitance increased by 195 %; and, (iii) for 4.5 V, where $\Delta V/V$ amounts to -4.0 %, it increased by 261 %. If the relative increase in capacitance were indeed equal to a relative increase in specific surface area, an increase by 261 % (i.e. by a factor of ~3.6) would imply an approximate decrease of the effective NCM622 particle diameter by ~3.6 (based on a simple cubic approximation, where the specific surface area would be inversely proportional to the length of the cube, if the total volume is kept constant), which in turn would imply an increase of the number of particles by a factor of ~50 (corresponding to the area change to the third power). Considering that the approximate size of the primary crystallites in the ~5–10 μm secondary agglomerates of the pristine NCM622 particles (see Fig. 3a) is ~0.1–0.5 μm, the above estimated increase in the number of particles would suggest that a significant fraction of the interfaces between the primary crystallites would be exposed to the electrolyte after this cycling procedure to 4.5 V due to crack formation. Assuming a mean diameter of roughly spherical primary crystallites of ~0.2 μm, their complete separation and the full exposure of their surface area to the electrolyte would correspond to a specific surface area of ~6 m^2/g_{AM}, which is ~20-fold higher than that of the pristine NCM622 material. As the maximum experimentally determined surface area increase upon cycling (see Fig. 6) is only ~3.6-fold, this suggests that a few hundred cycles within the here considered upper cutoff potentials does not lead to a complete disintegration of the secondary particle agglomerates.

Kr-BET surface area of cycled NCM622 electrodes.—To verify that an increase of the specific surface area of the NCM622 electrodes and particles is indeed the origin for their increased capacitance upon cycling, the surface area of cycled electrodes was measured by Kr-BET and compared with the observed capacitance increase. For this, the cells cycled to 4.5 V vs. Li^+/Li for which the first 203 cycles are shown in Fig. 5c (red symbols) were cycled for another 100 cycles (for cycling and capacitance data over 303 cycles, see Fig. S3); after 303 cycles, the cells were disassembled and the NCM622 electrodes were harvested and washed prior to the Kr-BET measurement. The specific capacitance was extracted from the impedance spectra of the pristine and the cycled NCM622 electrodes in blocking conditions (i.e. after a potential hold at 2.55 V vs. Li^+/Li), either by fitting of the *R-Q* element (hatched bars in Fig. 7) or by using the value of the imaginary impedance at 180 mHz according to Eq. 6 (solid bars in Fig. 7).

The specific capacitance of the NCM622 electrodes calculated from the 180 mHz point increases from 0.12 $F/g_{electrode}$ in their pristine state (solid bar on the left-hand side of Fig. 7) to 0.34 $F/g_{electrode}$ after 303 cycles to 4.5 V (solid bar on the right-hand side). Both determination methods for the electrode capacitance, the exact *R-Q* fit (hatched bars) as well as the 180 mHz approximation (solid bars),

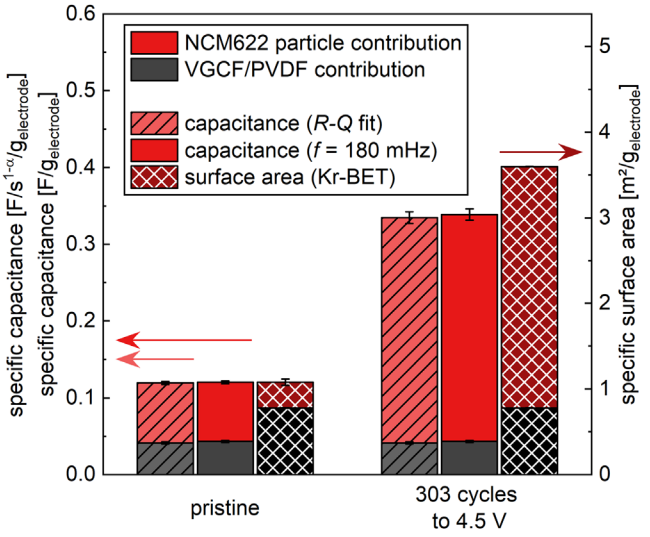

Figure 7. Effect of charge/discharge cycling on NCM622 electrodes for an upper cutoff potential of 4.5 V vs. Li^+/Li after 303 cycles, continuing the cycling shown in Fig. 5c (red symbols) for another 100 cycles (for cycling and capacitance data, see Fig. S3): Specific capacitances (left axis) of pristine electrodes (left-hand set of bars) and after the 203 cycles to 4.5 V vs. Li^+/Li (right-hand set of bars) were obtained either by fitting an *R-Q* element at frequencies between 100 mHz and 1 Hz (hatched bars) or by using the imaginary impedance at 180 mHz according to Eq. 6 (solid bars). BET surface area (right axis) of pristine and cycled NCM622 electrodes (cross-hatched bars) measured by Kr-BET. The contributions to capacitance and specific surface area by the NCM622 particles are colored in red and were obtained by subtracting the weight-fraction-normalized contributions from the VGCF electrodes (colored in black). All values are calculated from the mean of two nominally identical cells (capacitances) or two nominally identical electrodes (Kr-BET) and the error bars correspond to the minimum/maximum value of two measurements.

result in a very similar increase of the NCM622 electrode capacitance (left axis) over the 303 cycles, namely by 180 % and 182 %, respectively. This good agreement is expected, as the corresponding phase angles always exceed $\alpha = 0.85$, which was the requirement for the 180 mHz approximation (see Eq. 6) to be valid. Assuming that the contribution of the VGCF/PVDF components to the electrode capacitance remains constant upon cycling, the weight-fraction-normalized contribution from the VGCF electrode (i.e. 0.043 ± 0.001 $F/g_{electrode}$ or 0.041 ± 0.001 $F/s^{1-\alpha}/g_{electrode}$, constituting ~36 % of the total capacitance of the pristine NCM622 electrode) can be subtracted from the NCM622 electrode capacitance to obtain the NCM622 contribution to the capacitance (red colored parts of the bars in Fig. 7). Comparing the red colored segments of the hatched and solid bars for the pristine NCM622 electrode (left-hand side of Fig. 7) with those for the cycled NCM622 electrodes (right-hand side), a cycling-induced increase of the NCM622 capacitance contribution by ~280 % (i.e. by a factor of ~3.8) can be deduced.

The increase in NCM622 electrode and particle capacitance over the 303 cycles to 4.5 V vs. Li^+/Li will now be compared to the measured changes in the specific surface area determined by Kr-BET. The NCM622 electrode Kr-BET increases from 1.08 m^2/g (cross-hatched bar on the left-hand side of Fig. 7) to 3.6 m^2/g after 303 cycles (cross-hatched bar on the right-hand side). Subtracting the weight-fraction-normalized contribution of the VGCF/PVDF components to the specific surface area as explained in the discussion of Fig. 3d (i.e. 0.78 $m^2/g_{electrode}$, constituting ~72 % of the total specific surface area of the pristine NCM622 electrode), the specific surface area contribution of the NCM622 particles in the pristine NCM622 electrode can again be estimated to be 0.30 $m^2/g_{electrode}$ (corresponding to the Kr-BET area measured for pristine NCM622 active material). Here it should be noted that while in the case of the capacitance measurements in the non-intercalating electrolyte (10 mM TBATFSI in EC:

EMC 3:7 w/w) the ratio of the capacitance contribution of the NCM622 particles and the VGCF/PVDF components reflects the ratio of their Kr-BET areas (namely ~1:3 in both cases, see Fig. 3d), for the measurements in the intercalating LP57 electrolyte this ratio is ~2:1 for the capacitance contributions (hatched and solid bars on the left-hand side of Fig. 7) and ~1:3 for the Kr-BET area contributions (cross-hatched bar on the left-hand side of Fig. 7). This, we believe, can be explained by different dependencies of the capacitances of different materials (viz., NCM622 and VGCF) on the composition of the electrolyte. Assuming that the specific surface area of the VGCF/PVDF components will not be affected by cycling the electrodes, the specific surface area contribution of the NCM622 particles to the specific surface area of the electrode after 303 cycles can be estimated to be 2.82 $m^2/g_{electrode}$. This implies an estimated increase of the specific surface area of the NCM622 particles by 840 % (i.e. by a factor of ~9.4) over the 303 cycles.

Surprisingly, this estimated increase of the Kr-BET area of the NCM622 particles over the 303 cycles is ~2.5-fold higher than the above deduced capacitance increase of the NCM622 particles which was only a factor of ~3.8. This deviation might result from an unequal sensitivity of both methods towards the detectable surface area: As the size of krypton atoms is ~0.2 nm, pores which are larger than ~0.2 nm will contribute to the measured Kr-BET area, while only pores larger than ~1 nm will be accessible to the electrolyte (based on an estimated diameter of ~1 nm for solvated lithium ions) and will thus be able to contribute to the capacitance. Thus, the most likely explanation for the higher increase in Kr-BET area compared to the capacitance of NCM622 particles upon cycling would be the presence of very small pores or cracks in the cycled NCM622 particles, which are large enough to be detectable by Kr-BET, but too small for the wetting with electrolyte. If this assumption is true, the capacitance is a more meaningful measure for the electrochemically active surface area of an electrode as compared to the surface area obtained by Kr-BET, since the capacitance actually reflects the surface area in contact with electrolyte, which is the relevant area for the charge-transfer reaction as well as for possible side reactions, such as the attack of HF or dissolution of transition metals. The Kr-BET measurement also includes pores with a size between 1 nm and 0.2 nm, which, however, do not contribute to charge transfer and/or side reactions that require electrolyte contact. In addition to the different sensitivity of Kr-BET and capacitance, it cannot be excluded that the washing procedure which was applied to the cycled electrodes after disassembly of the cell prior to the BET measurements might have altered the obtained results as well, leading to the discrepancy between the surface area increase of the both techniques (note that such a washing step was not used for acquiring the data shown in Fig. 3d, where Kr-BET and capacitance measurements are essentially identical).

Additionally, the possible formation of a cathode electrolyte interphase (CEI) during cycling cannot be excluded; if it were to form, it could, in principle, change the areal capacitance (i.e. the capacitance normalized to the surface area of the electrode or of the cathode active material) and thereby compromise our here assumed direct correlation between the measured capacitance and the exposed surface area. However, the independently obtained evidence for crack formation and surface area increase by FIB-SEM and Kr-BET, respectively, prove that particle cracking and surface area increase indeed occur upon either mechanical compression or during cycling. In our view, the simplified assumption that the areal capacitance remains constant during crack formation (as stated in the theoretical considerations) seems to be a reasonable approximation. Nevertheless, the here suggested minor role of the changes in the areal capacitance of a cathode active material by the possible formation of a CEI upon cycling (or of an anode active material by the SEI formation upon cycling) is required to be investigated.

Summarizing the findings in this section, one can state that it was shown that electrochemical cycling of the NCM622 active material significantly increases its capacitance, which is most pronounced during the first few charge/discharge cycles. The capacitance increase is dependent on the chosen cutoff potential, since this defines the extent of volume change of the unit cells, that ultimately causes the cracking of the NCM secondary agglomerates. This has an important consequence for studies and analyses which involve a normalization of a measured property/signal to the specific surface area of the active material, which could lead to erroneous conclusions in cases where the specific surface area of cycled and/or compressed/calendered active materials increases substantially over that of the pristine active materials. Examples where this would be critical are rate tests where the current normalized to the surface area is crucial for the evaluation of the rate capability, the analysis of the charge-transfer resistance over the course of cycling, or the estimation of the thickness of a surface spinel or rock-salt structure from the amount of evolved gases.

Visual investigation of cycled NCM electrodes.—Figure 8 presents the cross sections of pristine NCM622 electrodes as well as of the ones harvested from cells cycled to 4.2 V vs. Li^+/Li after a first charge cycle at C/10, after the subsequent first discharge cycle at C/10 including a CV hold at 2.55 V vs. Li^+/Li, and in the charged state after the 203 cycles shown in Fig. 5 (according to the protocol shown in Fig. 2). The uncompressed pristine electrode (see Fig. 8a), as discussed before in the context of mechanical compression effects (see Fig. 3a), does not show any cracks through the secondary agglomerates. When the NCM622 electrode is charged in the very first cycle at C/10 to 4.2 V vs. Li^+/Li (see Fig. 8b), numerous cracks appear that are induced by the lattice volume contraction as well as by the anisotropic change of the lattice parameters *a* and *c*.[6,7] These cracks appear mainly in the radial direction of the particles, creating pathways that connect the outer part of the particles with the inner voids of the NCM622 particles. The largest of these newly formed pores show more than 1 μm in length, but no more than ~100 nm in width; however, the formed cracks are clearly wide enough to be penetrated by the carbonate-based electrolyte (i.e. wider than 1 nm).

At the end of the very first charge/discharge cycle including a final CV hold at 2.55 V vs. Li^+/Li, the FIB-SEM image depicted in Fig. 8c indicates that the NCM622 particles seem to have almost fully and reversibly expanded into their original state, i.e. that the cracks that had been visible in the charged state shown in Fig. 8b have largely been closed again. However, from the impedance analysis in the fully discharged state (i.e. after a 1 h CV hold at 2.55 V vs. Li^+/Li) at the end the very first charge/discharge cycle to 4.2 V vs. Li^+/Li, it was proven that the electrochemically active surface area has already increased by 47 % (second green symbol from the left in Fig. 6). This increase in area must originate from irreversibly opened cracks or pores that are large enough for electrolyte penetration (i.e. with a width of more than 1 nm), created either mechanically due to the volume change upon (de)lithiation or through the decomposition of residual lithium salts by protic species.[59] These cracks must, however, be too small to be visible in the FIB-SEM image (Fig. 8c), whereby it must be considered that if there were one single crack reaching to the center of the particle, the entire inner void volumes would be connected ionically and would thus substantially increase the electrochemically active surface area and capacitance.

The FIB-SEM image in Fig. 8d shows an NCM622 electrode in the charged state after 203 cycles to 4.2 V vs. Li^+/Li, revealing obvious irreversible cracks which must have formed due to the repeated volume change upon (de)lithiation. Compared to the first charge (see Fig. 8b), large cracks which cannot close anymore upon lithiation have formed in almost all NCM particles. Some particle fragments have even displaced from their original position in the secondary agglomerate, resulting in a permanent and irreversible surface area increase that must be accompanied by poor electronic contacting of some parts within the secondary agglomerate, since for some of the fragments only point contacts seem to provide an electronic pathway; some particle fragments might even be electronically fully isolated.[6,16,25–27] As mentioned above, the surface area of NCM622 cycled to 4.2 V vs. Li^+/Li for more than 200 cycles

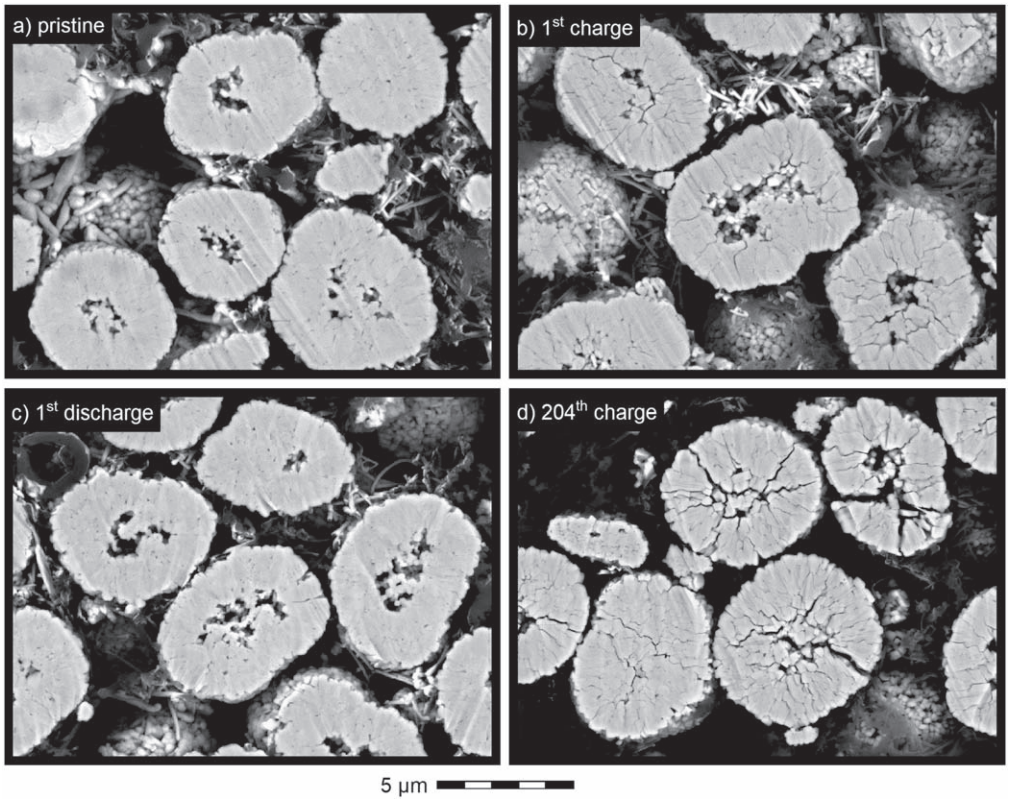

Figure 8. Visual investigation of particle cracking in uncompressed NCM622 electrodes upon charge/discharge cycling by cross-sectional FIB-SEM in backscattering mode at 10 kV. (a) Pristine electrode. (b) Partially delithiated/charged NCM622 electrode after the first charge at C/10 to 4.2 V vs. Li^+/Li. (c) Fully-lithiated/discharged NCM622 electrode at 0 %SOC after the first charge/discharge cycle at C/10 to 4.2 V vs. Li^+/Li followed by a 1 h CV hold at 2.55 V vs. Li^+/Li. (d) Partially delithiated/charged electrode at 4.2 V vs. Li^+/Li after the 203 cycles shown in Fig. 5.

increases by ∼200 % (green symbols in Fig. 6), corresponding to four complete cuts through the center of a sphere.

In summary, the FIB-SEM images, revealing the formation of cracks in the NCM622 secondary agglomerates and the formation of some almost completely isolated particle fragments upon repeated charge/discharge cycling, are consistent with the observed increase in NCM622 capacitance and Kr-BET surface area. While the latter two methods allow a more easy quantification of the extent of cracking, the FIB-SEM images also reveal that at least over the initial cycles, the cracking of the secondary NCM622 agglomerates seems to be partially reversible until larger and larger cracks are being formed over extended charge/discharge cycling. The additional electrochemically active surface area exposed through particle cracking has both detrimental and beneficial effects: On the one hand, these freshly created interfaces are expected to enhance side reactions and thus to lead to a loss of cyclable lithium and a loss of active material, reducing the battery cycle life. On the other hand, the formed cracks should facilitate the lithium-ion transport to the primary crystallites in the core of the secondary particles via fast transport through the lithium-ion conducting electrolyte (rather than through the solid phase), which will likely improve the rate capability of polycrystalline NCMs; since most of the cracking occurs within the first few cycles, the high rate capability of polycrystalline NCMs is likely due to their relatively high specific surface area (i.e. several times larger than what one would deduce from the BET area of the pristine materials). This latter aspect, when considering the case of all-solid-state batteries, however, is expected to have rather detrimental effects on performance and particularly on rate capability: As ion-conducting solid electrolytes or polymer electrolytes will not be able to intrude into the cracks formed in the NCM secondary particles, the transport of lithium ions into the interior of the secondary particles would be substantially hindered by the formation of cracks, so that crack formation would be expected to lead to a decrease of their capacity, particularly at higher C-rates. This indeed has been observed for all-solid-state batteries, e.g. based on polymer electrolytes as shown in the study of M. M. Besli.[66]

Electrochemical cycling of LFP and LTO.—To exclusively prove that the change in the unit cell volume leads to particle cracking and an increased electrochemical surface area, cycling experiments equivalent to the ones done for NCM622 were performed for two other active materials, namely LFP and LTO. LFP experiences a volume change of $\Delta V/V = -6.8$ % upon full delithiation,[62] causing stress and strain more than one order of magnitude higher as compared to LTO, which has a volume change of only +0.2 %;[61] moreover, for both of these active materials, the crystal structure is maintained upon cycling, since phenomena such as oxygen release have not been reported in contrast to NCM active materials. Furthermore, using LTO and LFP, intraparticular cracking can be investigated from a more fundamental perspective, since both materials are usually made up of individual primary crystallites instead of secondary agglomerates; therefore, an increase in capacitance would then correspond to a cracking of the primary particles rather than a convoluted effect resulting from a combination of intraparticular and interparticular cracking.

Figure S4 depicts the specific discharge capacity for both LFP and LTO working electrodes cycled according to the protocol shown in Fig. 2 against a pre-lithiated, capacitively oversized LTO as the counter electrode in Swagelok T-cells with a µ-RE (i.e. a GWRE). At C/10, LFP (green open symbols) provides 150 mAh/g_{AM} and loses 4 mAh/g_{AM} over 203 cycles, whereas LTO (yellow open symbols) exhibits 154 mAh/gAM with a capacity loss of 2 mAh/g_{AM} over 203 cycles, proving stable cycling for both materials over 203 cycles. However, both show a lower discharge capacity at 1C, by ∼20 mAh/g_{AM} for LFP (green filled symbols) and by ∼40 mAh/g_{AM} for LTO (yellow filled symbols). For LFP, the discharge capacity of

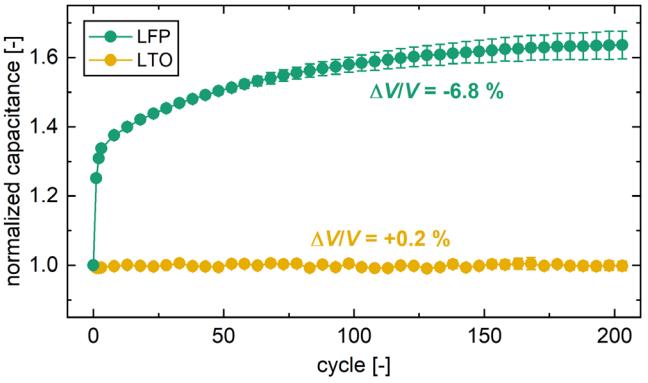

Figure 9. Capacitance of LTO and LFP working electrodes over extended charge/discharge cycling, determined from the imaginary impedance at a frequency of 180 mHz of the working electrodes under blocking conditions (using Eq. 6), normalized to the capacitance of the conditioning cycle (cycle #0). For this, pseudo full-cells were assembled in Swagelok T-cells with 60 µl LP57, two glass fiber separators, and a µ-RE (i.e. a GWRE) using LTO or LFP as working electrode and pre-lithiated, capacitively oversized LTO as the counter electrode. Following the procedure introduced in the experimental section and depicted in Fig. 2b, the cells were cycled at 25 °C, applying cutoff potentials of 1.05 and 2.05 V vs. Li^+/Li for LTO and 2.95 and 3.80 V vs. Li^+/Li for LFP. Impedance spectra of the working electrode were recorded after a potential hold at 2.55 V vs. Li^+/Li for both materials, applying an amplitude of 15 mV from 100 kHz to 100 mHz. The values shown here are calculated from the mean of two nominally identical cell pairs. The error bars correspond to the minimum/maximum value of two cells. The relative volume change of the unit cell upon delithiation as measured by XRD[7,61,62] (i.e. ΔV/V) is specified in the figure for both materials.

125 mAh/g_{AM} at 1C is reasonable.[67,68] For LTO, these losses can be attributed to a limited electronic conductivity through the electrode, since these electrodes were not compressed before cell assembly as compared to LFP. However, during the cycles at C/10, the full capacity was exchanged and, therefore, the entire volume change of the respective unit cell was achieved for both materials at least in these low-current cycles.

The capacitance upon cycling normalized to the value after the conditioning cycle (cycle #0) is depicted in Fig. 9 for both materials. The initial specific capacitance is 1.65 F/$g_{electrode}$ for the LFP electrode and 0.14 F/$g_{electrode}$ for the LTO electrode (data not shown). The capacitance of LTO, measured at 0 %SOC or full delithiation, shows no change over more than 200 charge/discharge cycles (green symbols). The relatively small volume change upon (de)lithiation of LTO, also often referred to as a zero strain material,[69] is not large enough to affect the mechanical stability of the material, and thus the formation of cracks has not been reported for LTO, which is reflected by the constant value of the electrode capacitance upon cycling.

For LFP, however, the capacitance of the electrode (yellow symbols, measured at 0 %SOC or full lithiation) increases by 25 % already after the first full cycle; over 203 cycles, the capacitance increases by a total of 64 % to 2.69 F/$g_{electrode}$. This surface area increase is expected to arise from the fracturing of the LFP particles, originating from the relatively large volume change of −6.8 % upon (de)lithiation, creating such large stress and strain that even the primary LFP crystallites are known to fracture.[67,70] In order to obtain the contribution of the capacitance of LFP to the total capacitance of the electrode, the contribution of C65 is subtracted from the capacitance of the LFP electrode, similarly done as for Figs. 3 and 6. However, since the weight fractions of C65 and PVDF in the LFP electrode are not 1:1, but 4:3, the calculations were adjusted in the following way: It was assumed that only C65 contributes to the capacitance of the C65/PVDF electrode, resulting in 3.5 F/g_{C65}. With this, the capacitance of C65 in the LFP electrode of 0.14 F/$g_{electrode}$ can be subtracted by considering the weight fraction of C65 in the LFP electrode (3 wt%) and assuming that its capacitance does not change over cycling (a reasonable assumption, as the C65 particles experience no ion (de)intercalation during cycling in this voltage region). With these assumptions, the capacitance of the LFP particles only increases by 71 % over 203 cycles. Gabrisch et al.[67] showed that LFP already forms first cracks upon a single chemical delithiation to 50 %SOC (corresponding to 0.25 charge/discharge cycles) due to the material's volume change, which explains the sudden increase in capacitance after the first charge/discharge cycle. Upon repeated cycling of LFP, some particles separate into two or more fragments, as found by TEM and SEM,[67,70] which can now by quantified in situ by our impedance-based analysis.

In summary, as illustrated by the overview in Table II, high surface area materials such as LFP, VGCF, and C65 result as expected in a relatively high specific capacitance as compared to LTO and NCM. Furthermore, the increase in capacitance upon cycling increases with relative volume change upon (de)lithiation, which is a general measure of particle cracking.

Table II. Overview of the major results. Relative unit cell volume change, specific capacitance of pristine electrodes (extracted from the capacitance at 2.55 V vs. Li^+/Li as shown in Fig. S2), capacitance increase of the various working electrodes after 203 cycles compared to the pristine electrodes, the active material surface area increase after having subtracted the contribution of conductive carbon to the electrode capacitance, as well as the capacity retention at C/10 and 1C. The specific capacitance and its increase are referred to the pristine material for NCM622 at 2.55 V vs. Li^+/Li and to cycle 0 for LTO and LFP. The relative volume change in the unit cell of each active material is taken from XRD measurements obtained from literature sources.[7,61,62] The error bars correspond to the minimum/maximum value of two cells.

		Electrode material						
	Units	NCM622 (3.9 V)	NCM622 (4.2 V)	NCM622 (4.5 V)	LTO	LFP	VGCF only	C65 only
Relative volume change	%	−1.0[7]	−1.8[7]	−4.0[7]	+0.2[61]	−6.8[62]	—	—
Spec. electrode capacitance (pristine)	F/g	0.12 ± 0.00	0.12 ± 0.00	0.12 ± 0.00	0.14 ± 0.00	1.65 ± 0.01	0.43 ± 0.01	1.73 ± 0.03
Electrode capacitance after 203 cycles	F/g	0.24 ± 0.00	0.27 ± 0.00	0.32 ± 0.01	0.14 ± 0.00	2.69 ± 0.06	—	—
Electrode capacitance gain over 203 cycles	%	+96	+125	+168	±0	+64	—	—
Active material surface area increase	%	+149	+195	+261	±0	+68	—	—
Capacity retention at C/10 over 203 cycles	%	99.6	88.5	80.8	—	—	—	—
Capacity retention at 1C over 199 cycles	%	94.4	84.8	78.5	—	—	—	—

Conclusions

In this paper, a novel in situ method based on impedance was introduced to monitor cracking of active material particles upon charge/discharge cycling. First, the analysis of impedance spectra in blocking conditions was illustrated from a theoretical point of view, showing that the electrode capacitance can be easily extracted at a frequency of 180 mHz to provide a measure of electrode surface area. The direct correlation of surface area and capacitance was validated by Kr-BET surface area measurements, and the cracking behavior of the NCM622 particles was observed by FIB-SEM. Over 200 cycles, the NCM622 active material showed a surface area increase of up to ∼261 % (i.e. by a factor of ∼3.6), depending on the upper cutoff potential. All studies in which electrochemical or analytical results are normalized to the surface area of an active material must consider this increase in surface area upon cycling, whereby the major gains in electrochemically active surface area are shown to occur during the first few cycles.

This novel method is highly beneficial as compared to post mortem Kr-BET measurements, symmetric cell measurements with harvested electrodes, or post mortem FIB-SEM analysis, since it can continuously track the surface area of a battery electrode in situ upon cycling at any point during extended cycle life tests. Therefore, this approach provides a powerful analytical tool to quantify particle cracking, thus facilitating quality management in CAM production. Moreover, it enables the monitoring of particle cracking originating from electrode calendering in cell production; thereby, the integrity of core–shell particles can be ensured, e.g. for NCMs synthesized with a radial gradient of the nickel content as well as for coated or gas-treated CAMs. Complementary studies specifically investigating the effects associated with the release of oxygen on the morphological integrity will be reported in Part II.

CrediT Authorship Contribution Statement

Stefan Oswald: Methodology, Investigation, Writing—Original Draft. Daniel Pritzl: Methodology, Supervision, Writing—Review & Editing. Morten Wetjen: Methodology, Supervision, Writing—Review & Editing. Hubert A. Gasteiger: Conceptualization, Supervision, Writing—Review & Editing.

Acknowledgments

Stefan Oswald and Daniel Pritzl gratefully acknowledge the BASF Battery Research Network for its financial support. Funding for Morten Wetjen was provided by the German Federal Ministry for Economic Affairs and Energy (BMWi; funding number 03ET6045D). BASF SE (Germany) is kindly acknowledged for providing the active materials, as are Dr. Manuel Mendez and Dr. Tobias Teufl for facilitating the FIB-SEM measurements at BASF. The authors also kindly thank Dr. Johannes Landesfeind, Robert Morasch, and Dr. Bharatkumar Suthar (all from TUM) for fruitful discussions.

ORCID

Stefan Oswald https://orcid.org/0000-0001-6402-7833
Daniel Pritzl https://orcid.org/0000-0002-9029-107X
Morten Wetjen https://orcid.org/0000-0002-2357-1151
Hubert A. Gasteiger https://orcid.org/0000-0001-8199-8703

References

1. D. Andre, S. J. Kim, P. Lamp, S. F. Lux, F. Maglia, O. Paschos, and B. Stiaszny, *J. Mater. Chem. A*, **3**, 6709 (2015).
2. S. T. Myung, F. Maglia, K. J. Park, C. S. Yoon, P. Lamp, S. J. Kim, and Y. K. Sun, *ACS Energy Lett.*, **2**, 196 (2017).
3. R. Schmuch, R. Wagner, G. Hörpel, T. Placke, and M. Winter, *Nat. Energy*, **3**, 267 (2018).
4. H. Noh, S. Youn, C. Seung, and Y. Sun, *J. Power Sources*, **233**, 121 (2013).
5. R. Jung, M. Metzger, F. Maglia, C. Stinner, and H. A. Gasteiger, *J. Electrochem. Soc.*, **164**, A1361 (2017).
6. A. O. Kondrakov, A. Schmidt, J. Xu, H. Geßwein, R. Mönig, P. Hartmann, H. Sommer, T. Brezesinski, and J. Janek, *J. Phys. Chem. C*, **121**, 3286 (2017).
7. L. De Biasi, A. O. Kondrakov, H. Geßwein, T. Brezesinski, P. Hartmann, J. Janek, L. de Biasi, A. O. Kondrakov, H. Geßwein, T. Brezesinski, P. Hartmann, and J. Janek, *J. Phys. Chem. C*, **121**, 26163 (2017).
8. Y. Mao, X. Wang, S. Xia, K. Zhang, C. Wei, S. Bak, Z. Shadike, X. Liu, Y. Yang, R. Xu, P. Pianetta, S. Ermon, E. Stavitski, K. Zhao, Z. Xu, F. Lin, X.-Q. Yang, E. Hu, and Y. Liu, *Adv. Funct. Mater.*, **29**, 1900247 (2019).
9. M. Lang, M. S. D. Darma, K. Kleiner, L. Riekehr, L. Mereacre, M. Ávila Pérez, V. Liebau, and H. Ehrenberg, *J. Power Sources*, **326**, 397 (2016).
10. H. R. Kim, S. G. Woo, J. H. Kim, W. Cho, and Y. J. Kim, *J. Electroanal. Chem.*, **782**, 168 (2016).
11. J. M. Lim, T. Hwang, D. Kim, M. S. Park, K. Cho, and M. Cho, *Sci. Rep.*, **7**, 39669 (2017).
12. H.-H. Ryu, K.-J. Park, C. S. Yoon, and Y.-K. Sun, *Chem. Mater.*, **30**, 1155 (2018).
13. P. Yan, J. Zheng, J. Liu, B. Wang, X. Cheng, Y. Zhang, X. Sun, C. Wang, and J. G. Zhang, *Nat. Energy*, **3**, 600 (2018).
14. S. Watanabe, M. Kinoshita, T. Hosokawa, K. Morigaki, and K. Nakura, *J. Power Sources*, **258**, 210 (2014).
15. H. Kim, S. Lee, H. Cho, J. Kim, J. Lee, S. Park, S. H. Joo, S. H. Kim, Y.-G. Cho, H.-K. Song, S. K. Kwak, and J. Cho, *Adv. Mater.*, **28**, 4704 (2016).
16. H. Liu, M. Wolf, K. Karki, Y. S. Yu, E. A. Stach, J. Cabana, K. W. Chapman, and P. J. Chupas, *Nano Lett.*, **17**, 3452 (2017).
17. P. C. Tsai, B. Wen, M. Wolfman, M. J. Choe, M. S. Pan, L. Su, K. Thornton, J. Cabana, and Y. M. Chiang, *Energy Environ. Sci.*, **11**, 860 (2018).
18. U. H. Kim, D. W. Jun, K. J. Park, Q. Zhang, P. Kaghazchi, D. Aurbach, D. T. Major, G. Goobes, M. Dixit, N. Leifer, C. M. Wang, P. Yan, D. Ahn, K. H. Kim, C. S. Yoon, and Y. K. Sun, *Energy Environ. Sci.*, **11**, 1271 (2018).
19. H. H. Sun and A. Manthiram, *Chem. Mater.*, **29**, 8486 (2017).
20. J. Wandt, A. T. S. Freiberg, A. Ogrodnik, and H. A. Gasteiger, *Mater. Today*, **21**, 825 (2018).
21. A. T. S. Freiberg, M. K. Roos, J. Wandt, R. De Vivie-Riedle, and H. A. Gasteiger, *J. Phys. Chem. A*, **122**, 8828 (2018).
22. J. A. Gilbert, I. A. Shkrob, and D. P. Abraham, *J. Electrochem. Soc.*, **164**, A389 (2017).
23. S. Solchenbach, G. Hong, A. T. S. Freiberg, R. Jung, and H. A. Gasteiger, *J. Electrochem. Soc.*, **165**, A3304 (2018).
24. R. Jung, F. Linsenmann, R. Thomas, J. Wandt, S. Solchenbach, F. Maglia, C. Stinner, M. Tromp, and H. A. Gasteiger, *J. Electrochem. Soc.*, **166**, A378 (2019).
25. J. H. Kim, S. J. Kim, T. Yuk, J. Kim, C. S. Yoon, and Y. K. Sun, *ACS Energy Lett.*, **3**, 3002 (2018).
26. F. Friedrich, B. Strehle, A. T. S. Freiberg, K. Kleiner, S. J. Day, C. Erk, M. Piana, and H. A. Gasteiger, *J. Electrochem. Soc.*, **166**, A3760 (2019).
27. F. P. McGrogan, S. R. Bishop, Y.-M. Chiang, and K. J. Van Vliet, *J. Electrochem. Soc.*, **164**, A3709 (2017).
28. C. Schilcher, C. Meyer, and A. Kwade, *Energy Technol.*, **4**, 1604 (2016).
29. J. Kim, H. Lee, H. Cha, M. Yoon, M. Park, and J. Cho, *Adv. Energy Mater.*, **8**, 1702028 (2017).
30. A. Manthiram, J. C. Knight, S. T. Myung, S. M. Oh, and Y. K. Sun, *Adv. Energy Mater.*, **6**, 1501010 (2016).
31. J. Pan, Y. Sun, P. Wan, Z. Wang, and X. Liu, *Electrochem. Commun.*, **7**, 857 (2005).
32. Y. K. Sun, S. T. Myung, B. C. Park, J. Prakash, I. Belharouak, and K. Amine, *Nat. Mater.*, **8**, 320 (2009).
33. J. Li, J. Camardese, R. Shunmugasundaram, S. Glazier, Z. Lu, and J. R. Dahn, *Chem. Mater.*, **27**, 3366 (2015).
34. B. B. Lim, S. T. Myung, C. S. Yoon, and Y. K. Sun, *ACS Energy Lett.*, **1**, 283 (2016).
35. Z. Sun, D. Wang, Y. Fan, L. Jiao, F. Li, T. Wu, D. Han, and L. Niu, *RSC Adv.*, **6**, 103747 (2016).
36. H. Kim, M. G. Kim, H. Y. Jeong, H. Nam, and J. Cho, *Nano Lett.*, **15**, 2111 (2015).
37. J. Zheng, J. Zhang, P. Yan, C. Wang, W. Zhao, S. Chen, and W. Xu, USA Pat. US2017/0338471A1 (2017).
38. G. Liu, M. Li, N. Wu, L. Cui, X. Huang, X. Liu, Y. Zhao, H. Chen, W. Yuan, and Y. Bai, *J. Electrochem. Soc.*, **165**, A3040 (2018).
39. H. Li, J. Li, X. Ma, and J. R. Dahn, *J. Electrochem. Soc.*, **165**, A1038 (2018).
40. S. Solchenbach, D. Pritzl, E. J. Y. Kong, J. Landesfeind, and H. A. Gasteiger, *J. Electrochem. Soc.*, **163**, A2265 (2016).
41. D. Pritzl, A. E. Bumberger, M. Wetjen, J. Landesfeind, S. Solchenbach, and H. A. Gasteiger, *J. Electrochem. Soc.*, **166**, A582 (2019).
42. G. J. Brug, A. L. G. van den Eeden, M. Sluyters-Rehbach, and J. H. Sluyters, *J. Electroanal. Chem.*, **176**, 275 (1984).
43. J. Bisquert, G. Garcia-Belmonte, P. Bueno, E. Longo, and L. O. S. Bulhões, *J. Electroanal. Chem.*, **452**, 229 (1998).
44. U. Rammelt and G. Reinhard, *Electrochim. Acta*, **35**, 1045 (1990).
45. B. Hirschorn, M. E. Orazem, B. Tribollet, V. Vivier, I. Frateur, and M. Musiani, *Electrochim. Acta*, **55**, 6218 (2010).
46. M. E. Orazem, I. Frateur, B. Tribollet, V. Vivier, S. Marcelin, N. Pébère, A. L. Bunge, E. A. White, D. P. Riemer, and M. Musiani, *J. Electrochem. Soc.*, **160**, C215 (2013).
47. O. Haik, S. Ganin, G. Gershinsky, E. Zinigrad, B. Markovsky, D. Aurbach, and I. Halalay, *J. Electrochem. Soc.*, **158**, A913 (2011).
48. J. Landesfeind, D. Pritzl, and H. A. Gasteiger, *J. Electrochem. Soc.*, **164**, A1773 (2017).

49. N. Ogihara, S. Kawauchi, C. Okuda, Y. Itou, Y. Takeuchi, and Y. Ukyo, *J. Electrochem. Soc.*, **159**, 1034 (2012).
50. N. Ogihara, Y. Itou, T. Sasaki, and Y. Takeuchi, *J. Phys. Chem. C*, **119**, 4612 (2015).
51. J. Landesfeind, J. Hattendorff, A. Ehrl, W. A. Wall, and H. A. Gasteiger, *J. Electrochem. Soc.*, **163**, A1373 (2016).
52. J. E. B. Randles, *Discuss. Faraday Soc.*, **1**, 11 (1947).
53. C. Ho, I. D. Raistrick, and R. A. Huggins, *J. Electrochem. Soc.*, **127**, 343 (1980).
54. M. Ebner, F. Geldmacher, F. Marone, M. Stampanoni, and V. Wood, *Adv. Energy Mater.*, **3**, 845 (2013).
55. S. Meini, M. Piana, H. Beyer, J. Schwämmlein, and H. A. Gasteiger, *J. Electrochem. Soc.*, **159**, A2135 (2012).
56. D. R. Gallus, R. Schmitz, R. Wagner, B. Hoffmann, S. Nowak, I. Cekic-Laskovic, R. W. Schmitz, and M. Winter, *Electrochim. Acta*, **134**, 393 (2014).
57. D. C. Grahame, *Chem. Rev.*, **41**, 441 (1947).
58. M. Gaberscek, J. Moskon, B. Erjavec, R. Dominko, and J. Jamnik, *Electrochem. Solid-State Lett.*, **11**, A170 (2008).
59. A. T. S. Freiberg, J. Sicklinger, S. Solchenbach, and H. A. Gasteiger, *Electrochim. Acta*, **346**, 136271 (2020).
60. R. Jung, P. Strobl, F. Maglia, C. Stinner, and H. A. Gasteiger, *J. Electrochem. Soc.*, **165**, A2869 (2018).
61. S. Scharner, W. Weppner, and P. Schmid-Beurmann, *J. Electrochem. Soc.*, **146**, 857 (1999).
62. A. K. Padhi, K. S. Nanjundaswamy, and J. B. Goodenough, *J. Electrochem. Soc.*, **144**, 1188 (1997).
63. T. Ohzuku, H. Tomura, and K. Sawai, *J. Electrochem. Soc.*, **144**, 3496 (1997).
64. K. Rhodes, N. Dudney, E. Lara-Curzio, and C. Daniel, *J. Electrochem. Soc.*, **157**, A1354 (2010).
65. A. Tranchot, H. Idrissi, P.-X. Thivel, and L. Roué, *J. Power Sources*, **330**, 253 (2016).
66. M. M. Besli, S. Xia, S. Kuppan, Y. Huang, M. Metzger, A. K. Shukla, G. Schneider, S. Hellstrom, Christensen, M. M. Doeff, and Y. Liu, *Chem. Mater.*, **31**, 491 (2019).
67. H. Gabrisch, J. Wilcox, and M. M. Doeff, *Electrochem. Solid-State Lett.*, **11**, A25 (2008).
68. V. Sharova, A. Moretti, T. Diemant, A. Varzi, R. J. Behm, and S. Passerini, *J. Power Sources*, **375**, 43 (2018).
69. N. Nitta, F. Wu, J. T. Lee, and G. Yushin, *Mater. Today*, **18**, 252 (2015).
70. D. Wang, X. Wu, Z. Wang, and L. Chen, *J. Power Sources*, **140**, 125 (2005).